CHARACTERIZATION OF MOLYBDENUM OXIDE AND MAGNESIUM
DOPED ZINC OXIDE CHARGE TRANSPORT LAYERS DEPOSITED BY
SPUTTERING FOR HETEROJUNCTION SOLAR CELLS

A THESIS SUBMITTED TO
THE GRADUATE SCHOOL OF NATURAL AND APPLIED SCIENCES
OF
MIDDLE EAST TECHNICAL UNIVERSITY

BY

GENCE BEKTAŞ

IN PARTIAL FULFILLMENT OF THE REQUIREMENTS
FOR
THE DEGREE OF MASTER OF SCIENCE
IN
MICRO AND NANOTECHNOLOGY

JANUARY 2017

Approval of the thesis:

CHARACTERIZATION OF MOLYBDENUM OXIDE AND MAGNESIUM DOPED ZINC OXIDE CHARGE TRANSPORT LAYERS DEPOSITED BY SPUTTERING FOR HETEROJUNCTION SOLAR CELLS

submitted by **GENCE BEKTAŞ** in partial fulfillment of the requirements for the degree of **Master of Science in Micro and Nanotechnology, Middle East Technical University** by,

Prof. Dr. Gülbin Dural Ünver   _____
Dean, Graduate School of **Natural and Applied Sciences**

Assoc. Prof. Dr. Burcu Akata Kurç   _____
Head of Department, **Micro and Nanotechnology**

Asst. Prof. Dr. Selçuk Yerci   _____
Supervisor, **Micro and Nanotechnology, METU**

Assoc. Prof. Dr. Alpan Bek   _____
Co-Supervisor, **Physics Dept., METU**

Examining Committee Members:

Prof. Dr. Çiğdem Erçelebi   _____
Physics Dept., METU

Asst. Prof.Dr. Selçuk Yerci   _____
Micro and Nanotechnology, METU

Prof. Dr. Raşit Turan   _____
Physics Dept., METU

Prof. Dr. Mehmet Parlak   _____
Physics Dept., METU

Assoc. Prof. Dr. Savaş Sönmezoğlu   _____
Metallurgical and Materials Eng. Dept., KMU

                                                         Date: 30.01.2017

I hereby declare that all information in this document has been obtained and presented accordance with academic rules and ethical conduct. I also declare that, as required by these rules and conduct, I have fully cited and referenced all material and results that are not original to this work.

Name, Last name: Gence BEKTAŞ

Signature :

iv

ABSTRACT

CHARACTERIZATION OF MOLYBDENUM OXIDE AND MAGNESIUM DOPED ZINC OXIDE CHARGE TRANSPORT LAYERS DEPOSITED BY SPUTTERING FOR HETEROJUNCTION SOLAR CELLS

BEKTAŞ, Gence

M.S., Micro and Nanotechnology

Supervisor: Asst. Prof. Dr. Selçuk Yerci

January 2017, 65 pages

Group IV semiconductors can easily be doped by group III and V elements to possess p and n type behavior, respectively, which enables homojunction solar cell designs. However, most of the compound semiconductors including CIGS, CdTe and perovskite can intrinsically be either n or p type. Therefore, heterojunction structures with well-aligned conduction bands between the absorber and electron transport layer (ETL) and well-aligned valence bands between the absorber and hole transport layer (HTL) are required. This thesis aims to investigate structural, optical and electrical properties of molybdenum oxide (MoO_x) HTL and magnesium-doped zinc oxide ($Zn_xMg_{1-x}O$) ETL fabricated by reactive rf magnetron co-sputtering for heterojunction solar cells. MoO_3 is a semiconductor with a band gap of 3.3 eV; however, defect states in oxygen-deficient MoO_x make it act like a high work function metal. In this study, oxygen vacancies were created both by stoichiometry control during deposition and by post annealing. Defect states formation near the valance band edge and its influence on work function of the material were analyzed by X-ray photoelectron spectroscopy (XPS). Crystallographic properties of MoO_x films were examined by X-ray diffraction (XRD). Refractive indices, extinction

v

coefficients and thicknesses of thin films were determined by spectroscopic ellispsometry. Finally, transmittance and reflectance spectra of MoO_x thin films were measured. ZnO_x is an alternative ETL to replace conventional ones due to its relatively low cost and high electrical conductivity. In this study, band gap of $Zn_xMg_{1-x}O$ was altered by Mg doping. Optical band gap studies were conducted by Tauc plot analysis using transmission spectra. Crystal structures of the samples were measured by XRD to illustrate adverse effect of Mg doping and healing effect of introducing oxygen during deposition. Spectroscopic ellipsometry characterization was performed to determine optical constants of thin films. Finally, perovskite solar cells were fabricated using sputtered ZnO_x.

ÖZ

HETEROEKLEM GÜNEŞ HÜCRELERİ İÇİN SAÇTIRMA YÖNTEMİ İLE BÜYÜTÜLMÜŞ MOLİBDAN OKSİT VE MAGNEZYUM KATKILI ÇİNKO OKSİT YÜK TAŞIYICI TABAKALARIN KARAKTERİZASYONU

BEKTAŞ, Gence

Yüksek Lisans, Mikro ve Nanoteknoloji

Tez Yöneticisi: Yard. Doç. Selçuk Yerci

Ocak 2017, 65 sayfa

Grup IV yarı iletkenleri, grup III ve V elementleri ile katkılanması sonucunda sırasıyla p ve n tipi davranışa sahip olması, ilgili katmanların çoklueklem güneş hücresi yapılarında kullanımına olanak sağlamaktadır. Buna karşın hali hazırda kullanılan birçok, CIGS, CdTe ve perovskit gibi, bileşik yapısındaki yarı iletken kendiliğinden, n ya da p tipi malzeme davranışına sahiptir. Bu nedenle, çoklueklem yapılarda soğurucu ve elektron taşıyıcı katmana (ETK) ait iletkenlik bantlarının ve soğurucu ve delik taşıyıcı katmana (DTK) ait değerlik bantlarının düzgün bir hizalanmaya sahip olması gerekmektedir. Bu tez çalışmasında, çoklueklem güneş hücrelerinde kullanılmak üzere, reaktif rf manyetron saçtırma yöntemi ile üretilen molibden oksit (MoO_x) DTK ve magnezyum katkılı çinko oksit ($Zn_xMg_{1-x}O$) ETK'larının yapısal, optik ve elektriksel özelliklerinin araştırılması amaçlanmıştır. Oksijen-eksikli MoO_x'teki kusur seviyeleri molibden oksidin yüksek iş fonksiyonuna sahip bir metal gibi davranmasını sağlar. Bu çalışmada molibden oksitteki oksijen eksikliği büyütme esnasında ve sonrasındaki ısıl tavlama ile oluşturulmuştur. Değerlik bandı yakınında oluşan kusur seviyeleri XPS ile analiz edildi. MoO_x'in kristalografik özellikleri XRD ile; kırılma indeksi, sönüm katsayısı ve film

kalınlıkları ise spektroskopik elipsometri ile belirlendi. Son olarak, üretilen MoO_x ince filmlerinin yansıma ve geçirgenlik tayfları ölçüldü. ZnO_x düşük maliyeti ve yüksek elektrik iletkenliği sebebiyle yaygın kullanılan ETK'ların yerini almak için iyi bir alternatiftir. Bu çalışmada, bileşik içindeki Mg katkı seviyesi değiştirilerek malzemenin bant aralığının ayarlanması amaçlanmıştır. Optik bant aralığı çalışmaları geçirgenlik verilerinin Tauc analiziyle yapıldı. $Zn_xMg_{1-x}O$ filmlerinin optik katsayıları ve film kalınlıkları spektroskopik elipsometri ile belirlendi. ZnO_x ETK kullanılarak perovskit güneş hücreleri üretildi.

Anahtar kelimeler: elektron taşıyıcı tabaka, delik taşıyıcı tabaka, MoO_x, $Zn_xMg_{1-x}O$, çoklueklem güneş hücreleri

Dedicated to my family

ACKNOWLEDGEMENTS

TABLE OF CONTENTS

LIST OF FIGURES

FIGURES

xiv

LIST OF TABLES

TABLES

NOMENCLATURE

HTL	Hole transport layer
ETL	Electron transport layer
PV	Photovoltaics
$E_{built-in}$	Built in electric field
CIGS	Copper indium gallium sulfide
CZTS	Copper zinc tin sulfide
CdTe	Cadmium telluride
CB	Conduction band
E	Energy
E_G	Energy band gap
FF	Fill factor
HF	Hydrofluoric acid
IPA	Isopropanol alcohol
DI	Deionized
I_{SC}	Short circuit current
ITO	Indium doped tin oxide
FTO	Fluorine doped tin oxide
J_{SC}	Short circuit current density
R	Reflectance
R_S	Series resistance
R_{SH}	Shunt resistance
T	Transmittance
TCO	Transparent Conductive Oxide
V	Voltage
VB	Valence band
V_{oc}	Open circuit voltage
XPS	X-ray photospectroscopy
XRD	X-ray diffraction
PCE	Power conversion efficiency

Zn	Zinc
ZnO	Zinc oxide
Mg	Magnesium
MgO	Magnesium oxide
Mo	Molybdenum
MoO_x	Molybdenum oxide
E_F	Fermi energy
n	Refractive index
k	Extinction coefficient
Cu	Cupper
CuO	Cupper oxide
PCBM	Phenyl-C61-Butyric-Acid-Methyl-Ester
P3HT	Poly(3-hexylthiophene-2,5-diyl)
RTA	Rapid thermal annealing
UV/O_3	Ultraviolet-ozone
ALD	Atomic layer deposition

CHAPTER 1

INTRODUCTION

The demand for photovoltaic (PV) technology keeps rising very steadily due to the problems with primary power resources. Developing industrialization and the growth in world population which was reported as 7.4 billion in 2006 bring about the lack of energy resources [1]. Besides, environmental issues are arising very remarkably due to these factors.

At the present time, the energy consumption by human being is mostly supplied by fossil fuels. However, developing renewable energy resources get increasingly popular and is expected to replace fossil fuels in the near future. The power generation from renewable energy resources in 2015 has grown from 0.8% to 2.8% less than in a decade. Wind energy constitutes the largest area in the global renewable energy generation chart by accounting for 52.2%. Nevertheless, solar energy had the highest growth rate in power generation by 32.6% increment while that in wind energy was only 17.4% in the 2015 [2]. Relying on this fact, harvesting energy from the sun seems to be one of the most promising resources.

PV technology historically dates back to the discovery of photovoltaic effect observed by Alexandre Edmond Becquerel in 1839. He stated that shining light onto an electrode in a conductive solution would create electric current. However, development of PV power did not continue very rapidly up until the discovery of photoconductivity of selenium (Se). In 1873, Willoughby Smith observed that selenium creates electricity when light was shone onto it. Nevertheless, it was

Charles Fritts who coated selenium with gold and managed to make the first solar cell with 1-2% efficiency.

One of the milestones of PV technology was the explanation of photoelectric effect by Albert Einstein in 1905. Although it had been observed by Heinrich Hertz in 1887, he could not explain this phenomena, which is very important in understanding light and electricity relation [3].

In 1904, semiconductor junction solar cell with copper (Cu) and copper oxide (CuO) was invested by Hallwachs without understanding the exact operational principle. After a long time, first single junction solar cell, which was based on silicon p-n junction, was developed by Daryl Chapin *et al.* at Bell Laboratory in 1954. The ancestor of solar cells, which was able to achieve 6% power conversion efficiency (PCE) at that time, is classified as the first generation solar cells [4]. Since then, researchers have been engineering various materials and designs in order to exceed the limits in PV technology. Therefore, second generation solar cells emerged with promising PCE performances up to 28.8% efficiency. Thin film solar cells in this generation consist of amorphous silicon, copper indium gallium selenide (CIGS) and cadmium telluride (CdTe) semiconductors. After that, third generation solar cells which includes organic photovoltaics (OPV), quantum dot photovoltaics, dye-sensitized solar cell and lastly perovskite solar cells, came up with appealing features such as mechanical flexibility, low-cost and ease of fabrication. The potential of tandem solar cells in the third generation solar cells to overcome Shockley-Queisser efficiency limit also received a lot of attention [5]. In the last decade, especially perovskite appeared to be very interesting material to be used in solar cells which have rooted from the idea of organic and dye sensitized solar cells. Perovskite solar cells, which have heterojunction structure, became hot topic in the research field with incredibly rapid improvement from 2% efficiency in 2006 to over 22% in 2016% [6].

Heterojunction solar cells are named as standard (non-inverted) or inverted structure depending on fabrication steps as shown in Figure 1.1.
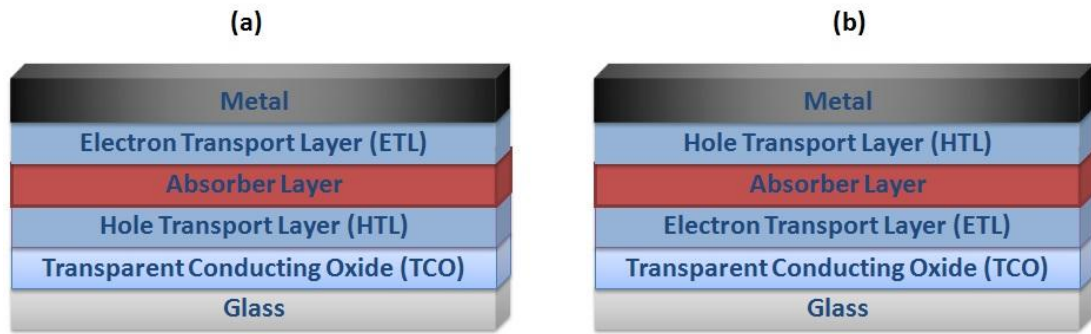
Figure 1.1. (a) Schematics of standard (non-inverted) and (b) inverted heterojunction solar cell

1.1. Operational mechanism of heterojunction solar cells

Solar cells can be designed in either homojunction or heterojunction structures. Homojunction is based on junction formation by doping of group IV elements with the ones from group III and group V which results in p and n type behavior, respectively. Transportation of charge carriers to electrodes are assisted by a built in electric field ($E_{built-in}$) in the depletion region created by diffusion of p and n-type materials. On the other hand, most of the compound semiconductors such as copper zinc tin sulfide (CZTS), copper indium gallium sulfide (CIGS), cadmium telluride (CdTe) and perovskite cannot be doped like group IV semiconductor elements. Therefore, heterojunction structure is needed for such semiconductors to create depletion region. Heterojunction is defined as the interface of two semiconductors with different energy band structure. In order to create $E_{built-in}$ in the depletion region, energetically asymmetric structure is provided by electrodes with different electron affinities. However, proper band alignment and low density of defect states in the heterojunction is needed to have a superior charge separation. In this regard, materials selection and engineering are crucial for charge transport layers in heterojunction solar cells.
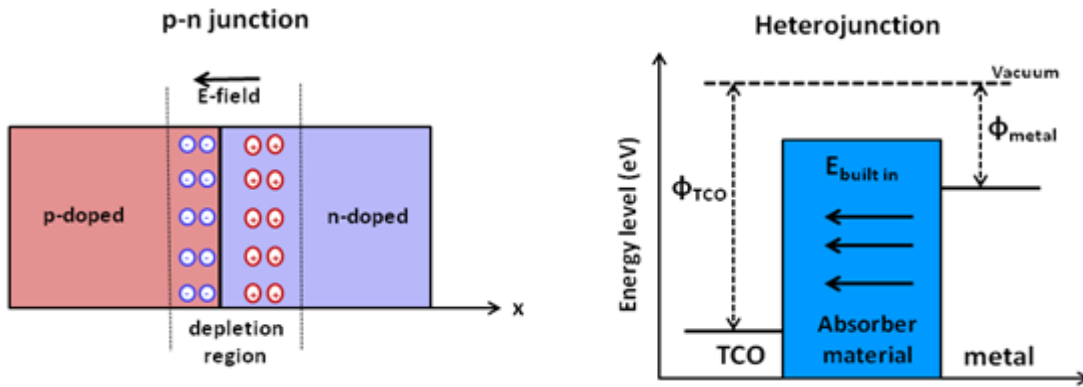
Figure 1.2. Illustration of p-n junction (on the left) and heterojunction structure (on the right)

In a heterojunction solar cell, an absorber material is generally placed between charge transport layers for improving energy band alignment and reducing recombination which is partially resulted from lattice mismatches. Typically, one of the charge transport layers is in touch with a metal electrode and another one form interface to a transparent conducting material depending on the design of current flow mechanism. When light is shone onto device, photons reaching photoactive semiconductor material create electron and hole pairs which are consequently collected by charge transport layers. Charge flow mechanism is determined by electron affinities of the electrodes and band alignment between layers.

In dark, all components of a conventional heterojunction solar cell are at equilibrium so that net charge flow through the circuit is ideally zero. In the case of inverted structure, the Fermi level of TCO is equilibrated with that of HTL as illustrated in Figure 1.3.
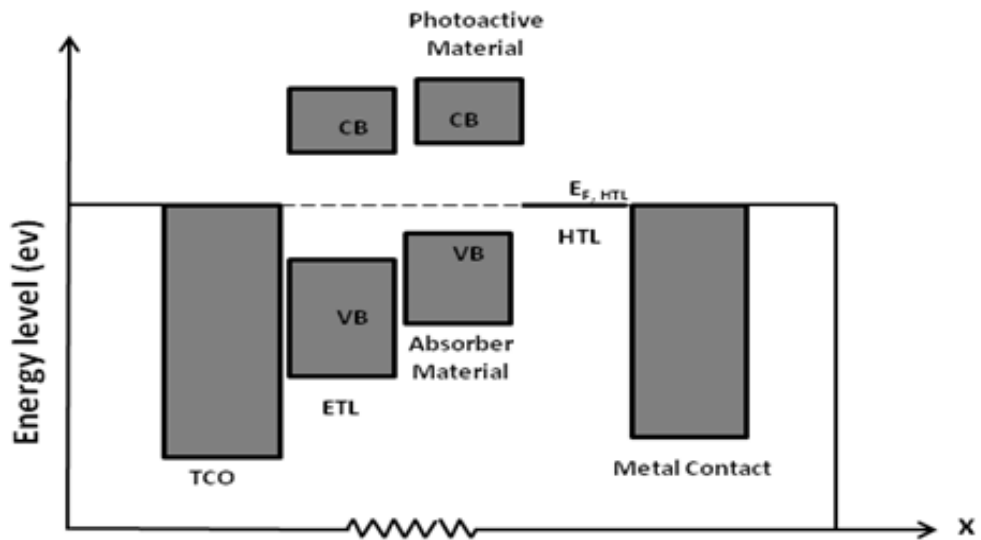
Figure 1.3. Energy band alignment of a heterojunction solar cell in dark

Under illumination, absorber layer absorbs photons with energies higher than its band gap and promotes electrons to its conduction band (CB) while passing down the holes to its valance band (VB) as in Figure 1.4. The promoted electrons in the CB of absorber material move to the CB of ETL and diffuse through TCO. On the other hand, the holes in the VB of absorber layer move to HTL and are collected by metal contact due to the difference in their work function. During electron flow from ETL to TCO, the CB of TCO moves upward by rising quasi-Fermi level due to electron accumulation. The difference between TCO quasi Fermi level and HTL quasi Fermi level is what determines the maximum open circuit voltage (max V_{oc}) [7].
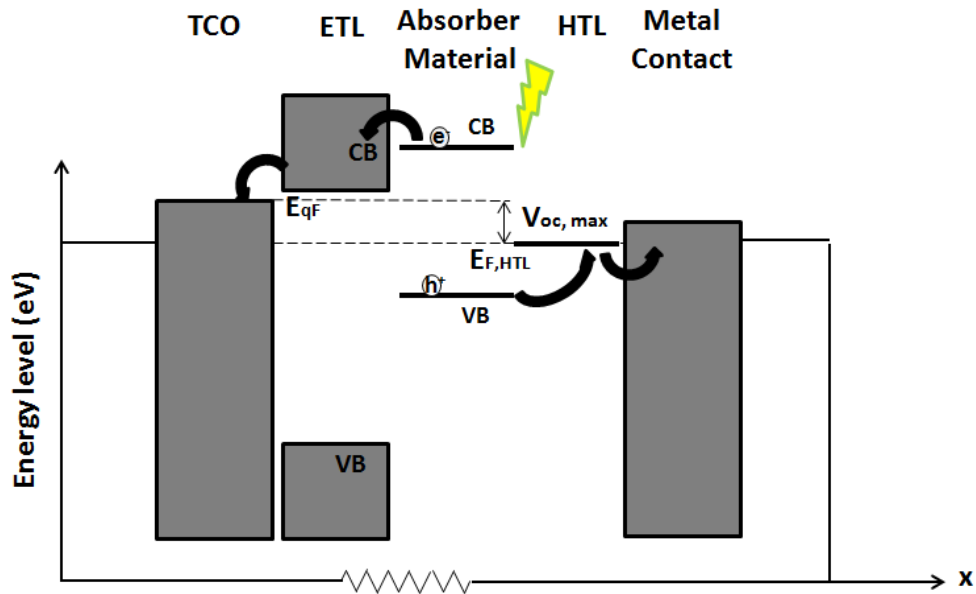
Figure 1.4. Energy band alignment of a heterojunction solar cell under illumination

In summary, heterojunction systems work in the existence of energetically asymmetrical design of electrodes and suitable band alignment of transport layers with adjacent materials. Because, built in electric field needs to be provided in the absorber material to drift electrons towards ETL and holes towards HTL.

1.2. Transparent conductive oxides

Transparent conductive oxides (TCOs) are extensively used in electronic and optoelectronic industry. Thanks to their optical transparency and their electrical conductivity, they are used as electrodes in flat-panel displays, light-emitting diodes, electro chromic windows and solar cells [8].

The first transparent conductive oxide, which is cadmium oxide (CdO), was reported by Badeker in 1907. Cadmium metal had been somehow oxidized and stayed conductive when it turned into transparent material. After invention of CdO, many TCO materials such as aluminum doped zinc oxide (AZO), indium doped tin oxide (ITO), and fluorine doped tin oxide (FTO) have emerged.

6

The use of TCOs as the front contact in photovoltaics has been comprehensively reviewed by Fortunato in 2007 [9]. High transparency and high conductivity are the most pronounced requirements for the front contact electrodes. While high transparency is necessary for photons to pass through TCO and reach absorber layer, conductivity is another important requirement to reduce Ohmic losses. Conductivity and energy band configuration of TCO can be controlled by doping concentration.

TCOs are designed for large area electrical contact on the front surface with conductivity greater than roughly 20 Ω·cm^{-1}. Also, high optical transparency in visible spectrum is aimed by wide-band gap oxides. Apart from wide band gap, work function of TCOs should be taken into consideration in case of heterojunction structures.

For heterojunction solar cells, FTO and ITO are the most preferred TCOs depending on cell design, material compatibility and energy band alignment. ITO has higher electrical conductivity and optical transmittance in visible wavelengths compared to FTO. However, ITO is not stable at high temperatures (approximately at 400 ^{o}C) and ends up with high electrical resistivity after post annealing [10]. In some cases, stability of a TCO at high temperatures is required. For example, TiO_2 deposited on TCO needs sintering over 450 ^{o}C for better crystallization to improve TiO_2 conductivity [11].

For an optimized TCO, an optimum free charge carrier concentration needs to be achieved for energy band alignment with adjacent materials. While high carrier concentration is required to achieve high conduction, high density of free charge carriers result in enhanced impurity scattering in the lattice and decrease electron mobility [12].

Nevertheless, optimization of TCO is not enough for effective charge collection through a heterojunction solar cell. The interface of two different materials called heterojunction always plays an important role in optical and electrical applications, as well. Because, two different crystal structures may end up with lattice mismatches which cause defects. These defects are account for dangling bonds acting as recombination centers and traps for free charge carriers. Lattice mismatch in the

7

interfaces of conventional TCOs and absorber materials such as perovskite, CZTS and CIGS materials are more frequent than that of available charge transport materials and absorber materials. In addition, electron transport layers such as ZnO_x and TiO_2 include less electron density with respect to TCOs such as ITO and FTO. Furthermore, low free charge density is needed in terms of reducing recombination of photogenerated holes and electrons through the materials which are adjacent to absorber material. From this point of view, it is quite important to select a suitable TCO material in a heterojunction structure for efficient charge transport mechanism by taking lattice structure and band alignment into consideration.

1.3. Charge Transport Mechanism and Energy Band Alignment

Energy band levels of materials and charge transport through them play critical roles in heterojunction solar cells. Under illumination, electrons in valance band of an absorber layer are excited to its conduction band. However, dissociation of electrons in excited energy states is achieved through an electric field, bulk trap sites or interface of materials with different electron affinities. In addition to given conditions for charge collection to respective electrodes, charge transport layers are also needed between electrodes and absorber layer to enhance dissociation and reduce recombination. In this regard, energy levels of materials which are connected to each other have to be taken into account so that the charge carriers can be collected with minimum losses. In other words, energy band alignment of charge transport materials is very important in dissociation of photogenerated electron-hole pairs.

Charge transport mechanism can take place in two different fashions which are electron dominated or hole dominated current flows. Energy levels of charge transport layers and that of respective electrodes determine which current flow will be dominant in the current mechanism. Two structures for charge transport mechanisms, which are hole flow only (left) and electron flow only(right), are illustrated in Figure 1.5 [13]. It illustrates how charge flow is directed by energy band alignment of materials.
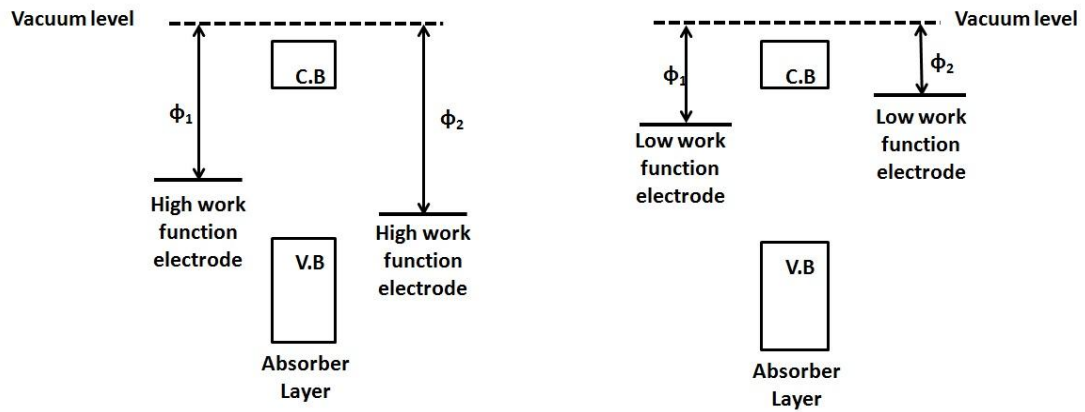
Figure 1.5. Hole only (left) and electron only (right) charge flow structure is depicted with energy states of materials

As a summary, it is possible to extract charges with both low work function materials and high work function materials, providing appropriate energy level configuration. For en efficient charge separation, electrons and holes should be selectively collected to opposite sides by electrodes with appropriate energy alignment as seen in Figure 1.6. Charge selection should also be enhanced with the assist of charge transport materials in the junctions. Therefore, it is needed to engineer energy band structures of conventional charge transport materials by creating controllable defect states or incorporation of various materials with different electronic characteristics, so that superior electron and hole separation can be provided.

Conduction band minimum and valance band maximum of commonly used absorber materials are given in Table 1.1. While engineering the energy band levels of the charge transport materials, one should take energy levels of absorber materials into account for efficient charge collection through the heterojunction structure.
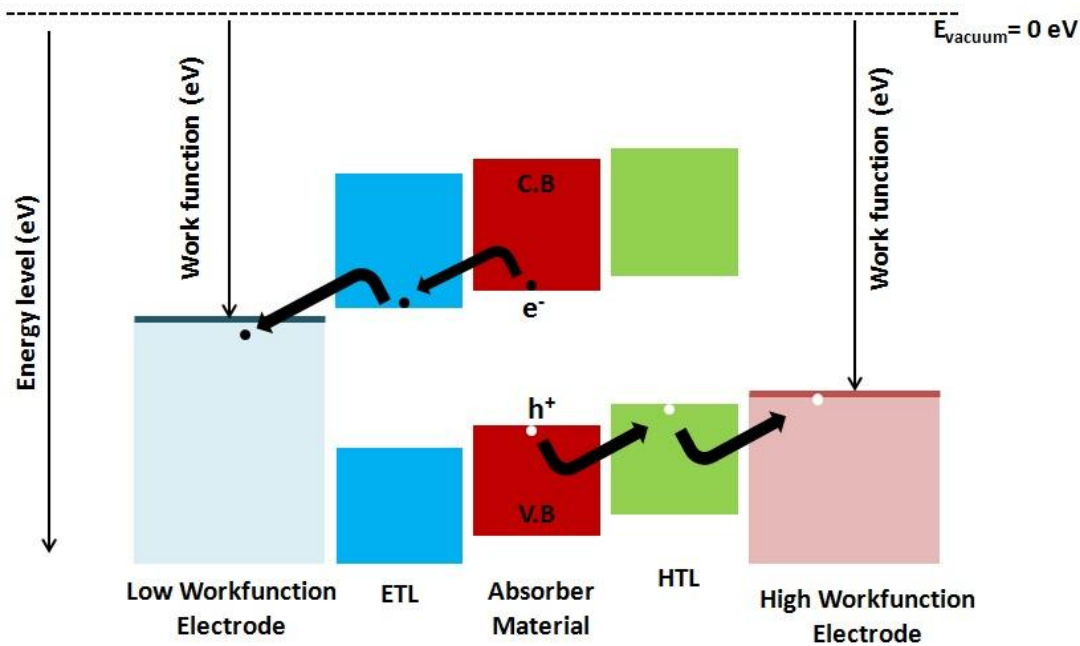
Figure 1.6. Schematics showing band alignment for efficient charge transport through heterojunction solar cell

Table 1.1. Energy band levels of conventional absorber materials currently used in heterojunction solar cells

Absorber Material	Conduction Band Minimum (eV)	Valance Band Maximum (eV)
Perovskite ($CH_3NH_3PbBr_3$)	-4.2	-6.5
Perovskite ($CH_3NH_3PbI_3$)	-4.2	-5.7
CZTS [14]	-3.79	-5.19
CIGS [14]	-4.25	-5.35
PTB7:PC71BM [15]	-3.3 (CB_{PTB7})	-6.1 (VB_{PCBM})
P3HT:PCBM [15]	-3.0 (CB_{P3HT})	-6.1 (VB_{PCBM})

1.4. Outline of this thesis

Chapter 1 summarizes how photovoltaic industry developed historically and explains the basics of heterojunction solar cells by making analogy to p-n junction. Also, the

use of transparent conducting oxides as electrodes in heterojunction structures is covered. Lastly, charge transport mechanism through a heterojunction structure is explained.

Chapter 2 includes the methods which were used to characterize charge transport layers fabricated by sputtering in this study. Firstly, UV/Vis. spectroscopy and ellipsometry are explained as optical characterization techniques. Then, X-ray diffraction (XRD) and X-ray photoelectron spectroscopy (XPS) are discussed to elucidate their working principles.

Chapter 3 is allocated to the discussion of transition metals, transition metal oxides and literature studies of MoO_x and $Zn_xMg_{1-x}O$ as charge transport materials.

Chapter 4 discusses results of our findings on MoO_x and $Zn_xMg_{1-x}O$ fabricated throughout this study.

CHAPTER 2

EXPERIMENTAL TECHNIQUES USED IN THIS STUDY

Thin films can be deposited by either physical or chemical deposition methods. Sputtering is categorized as a physical deposition technique and performed at the presence of a plasma which is gaseous mixture of negatively charged electrons and positively charged ions. Plasma is classified as one of the four states of matter. It is also called as quasineutral gas as density of negative and positive charges in macroscopic volume is in balance.

Plasma can be generated by thermal or cold means. For cold generation, direct current (DC) or radiofrequency (RF) power is applied at a very low pressure in the range of mTorr. While free electrons reach high temperatures, ions and neutral gas stay at low temperatures because of their large masses as compared to free electrons. Due to this inequality in temperature of the plasma, it is sometimes called as non-isothermal or non-equilibrium plasma. Although it is produced at low temperature, chemical reaction of molecules in the sputtering process is initiated with hot electrons.
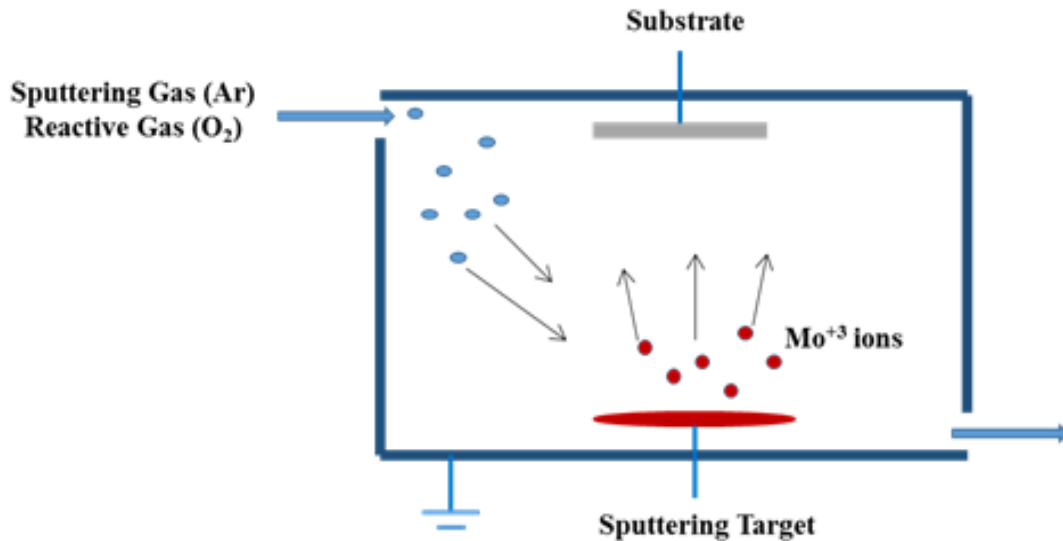
Figure 2.1. Schematics of magnetron sputtering

Plasma created in a vacuum chamber will result in ion bombardment on the surface of the target material. Ions hitting the surface can be reflected back, sticked, adsorbed, ejected, implanted to target or it can sputter surface atoms. Energy of ion beam determines its interaction with material by altering surface sticking probability. Possible reactions between an ion and a target material versus kinetic energy (temperature) of ion hitting the surface are illustrated in Figure 2.2. If energy of an ion is low enough, then it may stick to material by condensation or chemisorptions [16]. Moreover, it will be implanted into the material if energy of ion is too high. Sputtering regime is where sticking probability is lower than that of right before implantation regime.
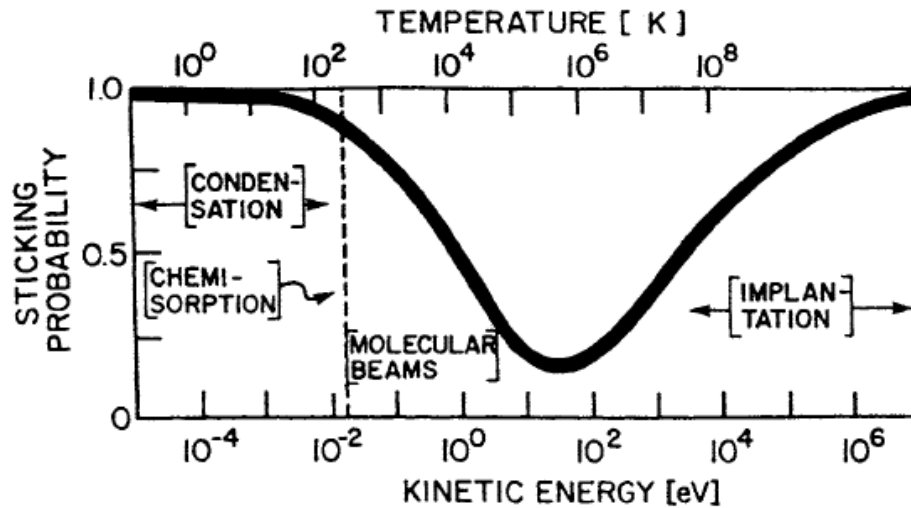
Figure 2.2. Particle-sticking probability as a function of energy. The dashed vertical line corresponds to room-temperature thermal energy [16]

In order to explain the mechanism of thin film deposition by sputtering technique, it is best to divide it into two sections, which are magnetron and reactive sputtering. Magnetron sputtering is performed by only inert gas to sputter the target material. On the other hand, reactive sputtering is proceeded with addition of reactive gas during deposition in order to form oxides, nitrides, carbides, etc. [17]. Magnetron sputtering is also classified in two groups which are DC and RF sputtering.

DC sputtering, which is also known as diode or cathodic sputtering, is used to sputter only metallic but not high resistive materials. In order to draw 1 mA/cm^2 current density across an insulator target with 10^{16} ohm-cm resistivity and 1 cm thickness, 10^{13}V voltage across the target will be dropped (V= ρjd; where ρ: resistivity, j:current density and d:thickness of target). Therefore, it is not possible to create plasma with such a high voltage drop across the target. RF power source with an impedance matching network, which is capable of sputtering even insulator target materials, is alternative to overcome this issue. Because, periodic reversal of polarity by RF voltage prevents charge build-up on a target.

Deposition rate for magnetron sputtering, which is pressure and current dependent, needs to be optimized for different target materials. If the pressure in the chamber is low, plasma will occur far from the target which reduces the sputtering rate. Also,

15

mean free path of electrons between collisions will be large and this will reduce secondary electron emission, which normally compensates electrons collected by anode. Also, if the deposition pressure is very high, sputtering rate would again decrease due to energy loss of scattered ions and electrons during collision as seen in Figure 2.3. A compromise between deposition rate versus deposition pressure has to be considered to make a correct deposition rate optimization [16].
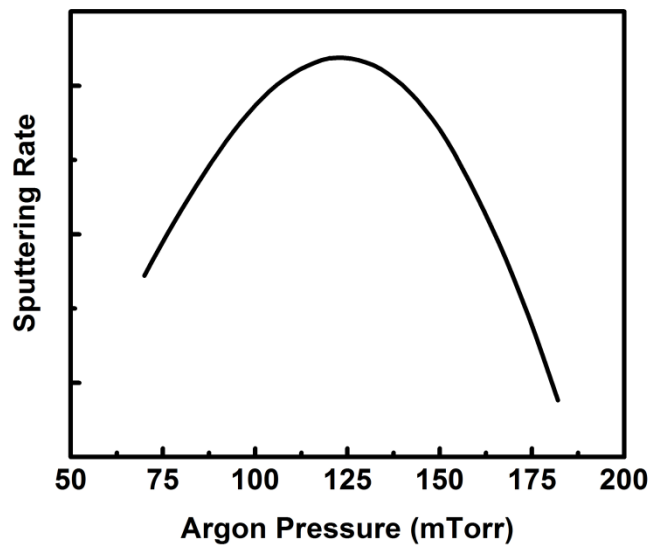
Figure 2.3. Representative sputtering rate versus argon pressure for magnetron sputtering

Reactive sputtering, on the other hand, has a different mechanism from magnetron sputtering. Not only film composition but also deposition rate totally changes with addition of reactive gas. Decreasing reactive gas flow rate does not track the same sputtering erosion rate curve, which is obtained by increasing reactive gas flow rate as seen in Figure 2.4. The reason for such a hysteresis behavior is resulted from compound formation on the sputtering target itself. As the target gets coated by compound of reactive gas and target material, sputtering rate decreases very slowly. When the surface of sputtering target reacts with reactive gas and totally coated with its compound, deposition rate falls drastically [18].

16
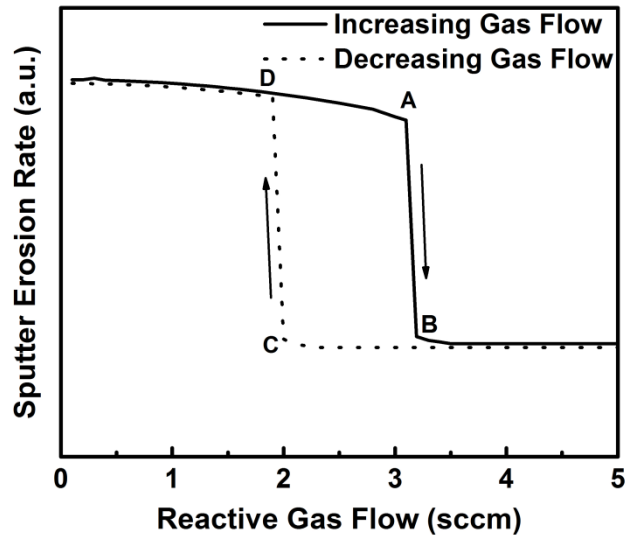
Figure 2.4. Sputter erosion rate versus reactive gas flow rate with arbitrary values

Thin films in this study were deposited by Nano-D sputtering system in GUNAM. Reactive magnetron sputtering and co-sputtering methods were used for sample fabrication.

2.1. Optical Characterization Methods

Optical spectroscopy is frequently applied for material analysis. The physics of these methods is based on the Bohr-Einstein frequency relationship.

$$\Delta E = E_2 - E_1 = h\nu, \qquad\qquad (Eq.\ 2.1)$$

where ΔE corresponds to discrete atomic or molecular energy states. According to Einstein's quantum theory, light consists of tiny particles called photons; while matter is composed of comparable size of particles which are called electrons, protons and neutrons. The equation tells that discrete energy levels of a matter can be linked to energy of a photon which has a frequency of ν by a proportionality constant, h, which is called Plank constant [19]. Ellipsometry and UV/Vis. measurement are only two of the optical characterization methods applied for optical characterization in this study.

17

2.1.1. Spectroscopic Ellipsometry

Ellipsometry is a non-destructive optical technique for refractive index, thickness, surface roughness, uniformity, isotropy, interfacial region, composition and crystallinity determination of various bulk materials and thin films. In ellipsometry, the change in polarization state of light after reflected from a surface of a single or multilayer film stacks is measured. Polarization status of light can be investigated in two steps which are change in the amplitude ratio (Ψ) and phase difference (Δ). During an ellipsometry measurement, incident electromagnetic wave is linearly polarized by a polarizer. When polarized light is reflected from a smooth surface, the light changes its state of polarization and becomes elliptically polarized, as illustrated in Figure 2.5. Therefore, it is named as ellipsometry.
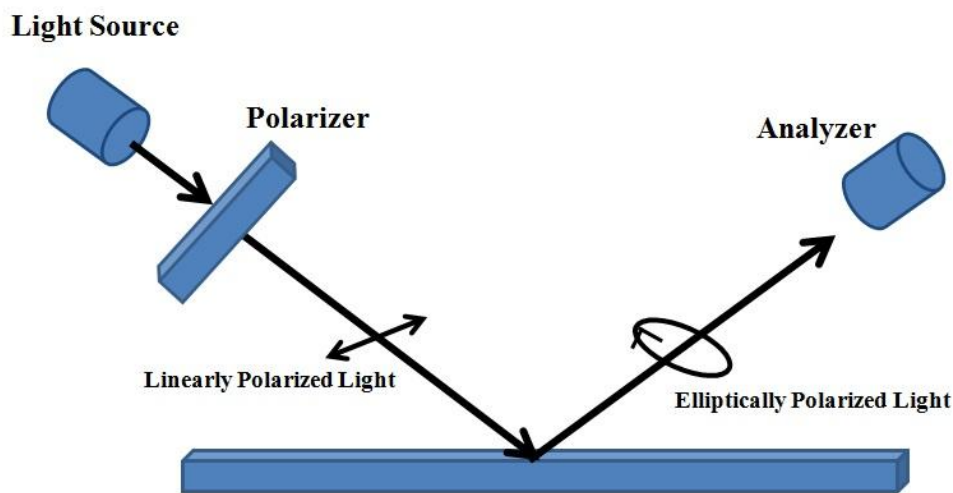
Figure 2.5. Schematics of ellipsometry measurement

It is an optical path sensitive technique and influenced from surface roughness and uniformity which results in depolarization of light. It dictates that the sample measured should be flat and the thickness of the film should be uniform all over the measured spot.

After measurement is done, an appropriate model should be applied for a correct data fitting and analysis. Therefore, it is necessary to have knowledge on the material

which will be analyzed so that suitable parameters can be estimated before construction of model. The model and the structure are supposed to meet some specific features that materials possess. Therefore, dispersion relationships need to be understood before implemented in a model. For instance; while some dispersion formulas such as Cauchy and Sellmeier are used for only transmitted wavelengths, some others such as Lorentz, Gaussian, Forouhi-Bloomer and Tauc-Lorentz can be applied for the spectrum where photons are absorbed [20]. Therefore, fitting on measured values of a material can be divided into two regions which are transparent and absorbing wavelengths. In long wavelengths, which are mostly transmitted by materials, thickness and refractive index are determined and they can be used to obtain k values by a suitable model.

In this study, Semilab located in GUNAM was used to conduct ellipsometry measurements. Delta and Psi values were measured with steps of 0.001 eV and measurement intervals were taken approximately between 400-1000 nm although it varied slightly depending on the samples. Cauchy and Sellmeier models were used to fit the measured values.

2.1.1.1 Cauchy Model:

Cauchy dispersion formula is used to describe index of refraction (n) of a material which has no absorption in measured wavelength interval.

In order to relate index of refraction and extinction coefficient, the empirical relations should be consistent with Kramers-Kronig relation. However, parameters of Cauchy formula are not physical and they are inconsistent with Kramers-Kronig relation. In other words, it is not very suitable for absorbing materials.

In the equation, B and C constants which determine the shape of dispersion curve. A is the dimensionless parameter which is equal to refractive index, $n(\infty)$, when $\lambda=\infty$.

$$n(\lambda)=A+B/\lambda^2+C/\lambda^4 \, , \qquad\qquad\qquad (Eq.\ 2.2)$$

where $k(\lambda)=0$. There is also another formulation of Cauchy equation which is "Cauchy Absorbing dispersion" and it is applied for transparent material with weak absorption. Cauchy Absorbent equation is given as the following;

19

$$n(\lambda)=A+B/\lambda^2+C/\lambda^4 \quad \& \quad k(\lambda)=D+E/\lambda^2+F/\lambda^4 \,, \qquad \text{(Eq. 2.3)}$$

where; D, E and F are the constants which are analogous to A, B and C [21].

2.1.1.2 Sellmeier Model:

Sellmeier is another model that can be applied to determine optical constants and thicknesses of transparent materials. When k = 0,

$$n^2(\lambda) = A + B \times \frac{\lambda}{\lambda^2 - \lambda_o^2} \,, \qquad \text{(Eq. 2.4)}$$

In the Equation 2.3, $A \; (1 \leq A)$ is a dimensionless parameter. It determines the refractive index at $\lambda=\infty$. B determines the shape of refractive index in visible range. λ_o is the resonance wavelength and fitting should not be performed at this wavelength. Because, it is the wavelength, at which refractive index diverges.

Sellmeier equation is formulated for transparent materials with very low extinction coefficients as in the case of Cauchy formula. Sellmeier formula is given as the following;

$$n^2(\lambda) = \frac{1+A}{1+\frac{10^4.B}{\lambda^2}} \,, \qquad \text{(Eq 2.5)}$$

where $n(\lambda) = \sqrt{1 + A}$ at $\lambda =\infty$.

$$k(\lambda) = \frac{C}{10^{-2}.n.D.\lambda+\frac{10^2.E}{\lambda}+\frac{1}{\lambda^3}} \,, \qquad \text{(Eq. 2.6)}$$

where, C is the strength of absorption coefficient curve. D and E are the constants which determine the increase or decrease in absorption. D and E are inversely proportional to absorption of the material [21].

2.1.2. UV/Vis Spectroscopy

UV/Vis. spectroscopy is based on photon absorption of a matter. Energy of a photon in near ultraviolet and visible region corresponds to excitation energy of electrons in outer shell. Therefore, UV/Vis. principally gathers information from electronic transition of a matter. On the other hand, characteristic of vibrational and rotational

transitional states of molecules do not give any information in UV/Vis spectrometer. Because, vibrational transition occurs with photons in near infrared region and rotational transition takes place with photons in far infrared or microwave range.

In order to comprehend UV/Vis spectrum, it is necessary to know the Beer's law, as well. According to the law, intensity of a light attenuates logarithmically during its travel through a material as the path length increases linearly [22].

The transmission behavior of a light through a material can be hypothetically represented as Figure 2.5.
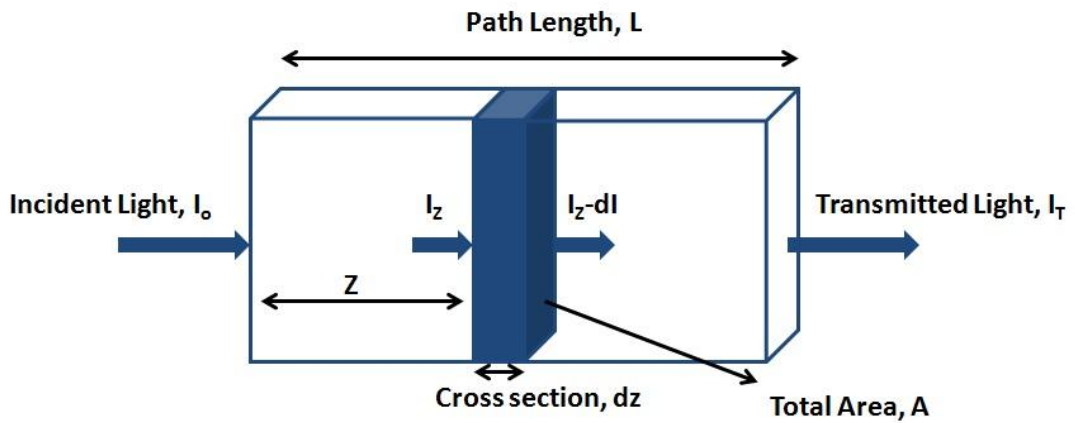
Figure 2.5. Transmission of light through a medium

For mathematical derivation of transmissivity, intensity loss of light propagating through a small slice of a medium can be written as;

$$dI = -\alpha dL \times I(z), \qquad \text{(Eq. 2.7)}$$

where α is the absorption coefficient of the medium. When dI is integrated, Beer's law is obtained as;

$$I(z) = I_o \, e^{-\alpha z} \;, \qquad \text{(Eq 2.8)}$$

where I_o is the intensity of incident light at z = 0.

UV/Vis. spectrophotometer setup basically consists of light source, entrance slit, collimating lens, chopper, integrating sphere, monochromator and detector.

UV/Vis. measurements in this study were carried out in GUNAM. Transmittance (T) and reflectance (R) were measured between 350 and 1100 nm with steps of 10 nm. Tauc analysis was applied to find band gap of fabricated samples.

Tauc Equation:

Tauc plot analysis is applied to determine the band gap from transmittance of a material. Mathematical derivation of Tauc formula is based on energy and momentum conservation of a photon absorbed by a medium. Hence, one should first write the energy of valance band (E_v) and conduction band (E_c) in momentum space (k) as the following equations,

$$E_v (k_v) = -\hbar^2 k_v^2/2m_v^* \ \& \ E_c (k_c) = E_g + \hbar^2 k_c^2/2m_c^*, \qquad (Eq.\ 2.9)$$

where $\hbar$: Planck constant, and m_v^* and m_c^*: effective masses in valance and conduction bands, respectively.

Momentum conservation in k-space is written as the following;

$$\hbar k_v^- + \hbar q^- = \hbar^2 k_c^- , \qquad (Eq.\ 2.10)$$

where k_v^- is wave vector in valance band and k_c^- is in conduction band for electron; q^- is the wave vector for absorbed photon. q^- is negligible with respect to momentum of the electron, and k_c^- is equal to k_v^- for momentum conservation.

For energy conservation, Eq. 2.11 needs to be satisfied;

$$E_v + \hbar\omega = E_c \ ; \ hence, \ E_c - E_v - \hbar\omega = 0 \qquad (Eq.\ 2.11)$$

Eq. 2.11 is written in the k-space the following,

$$E_g + \hbar^2 k_c^2/2m_c^* + \hbar^2 k_v^2/2m_v^* - \hbar\omega = 0 \ ;$$

If we define reduced mass as $1/m^* = 1/m_e^* + 1/m_v^*$, Eq. 2.12. is obtained.

$$E_g + \hbar^2 k^2/2m^* = \hbar\omega \qquad (Eq.\ 2.12)$$

22

Eq. 2.12 should be correlated with absorption coefficient (α) to obtain Tauc equation.

$$\alpha = \frac{(\hbar\omega)(\text{transition probability/volume time})}{\text{total incident intensity} \left(\frac{\text{energy}}{\text{unit time.area}}\right)},$$ (Eq. 2.13)

where total incident intensity is $\omega^2/8\pi c$.

When Eq. 2.12 and Eq. 2.13 are combined, Tauc equation for the direct band gap structure is obtained as the following;

$$(\alpha\hbar\omega)^2 = (\hbar\omega - E_g)$$ (Eq. 2.14)

Eq. 2.14 implies that optical band gap of a material can be deduced from linear fitting of $(\alpha\hbar\omega)^2$ versus $\hbar\omega$ graph [23].

2.2. X-ray Diffraction (XRD)

One of the extensive uses of X-rays is to obtain information on atomic structural arrangements. X-ray, which is in the order of atomic spacing of a crystalline solid, is diffracted when it interacts with a matter due to its wave characteristics.

Atomic structure information of crystalline solid can be acquired through X-ray, electron and neutron as long as they have wavelengths in the range of 0.1 to 10 °A. In case of X-ray, it is not possible to observe atoms directly due to lack of lens system which can focus X-rays. However, its interference effect is interpreted after scattered by atoms of a crystal lattice.

According to Bragg, an incident monochromatic X-ray is reflected from scattering centers, which is formed by planes of atoms. For constructive interference, the condition below has to be satisfied:

$2d\sin\theta = m\lambda$ where $m = 1,2,3 \dots$ and d is the atomic spacing between atomic planes [24].
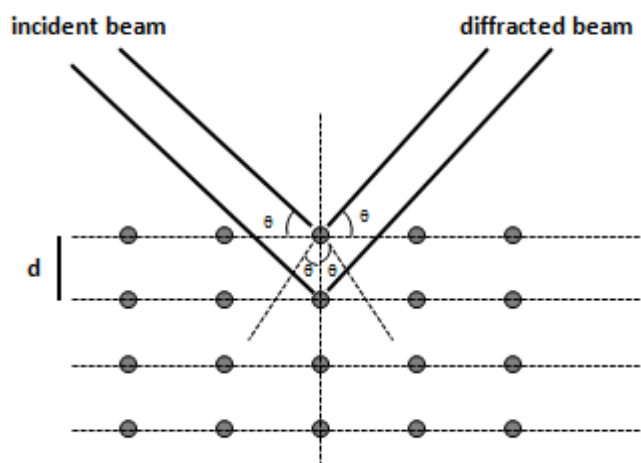
Figure 2.6. X-ray diffraction from a crystal

For XRD measurement, X-ray is radiated onto a sample which is positioned on a rotating table as seen in Figure 2.7. Intensity of diffracted X-rays are measured at different angles as the table is rotated. X-ray detector counts diffracted X-ray intensity (counts/sec.) for each angle and intensity versus 2θ (^{o}) is obtained.
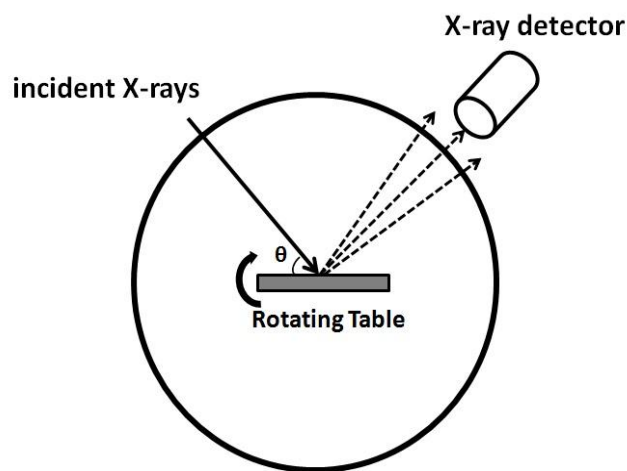
Figure 2.7. Schematics of X-ray diffraction (XRD) system

XRD measurements were carried out in GUNAM by Rigaku Miniflex XRD system equipped with CuK_α radiation of average wavelength of 1.54059 ^{o}A. Each samples were scanned between 0° and 90° with scan speed of 4 degree/min and steps of 0.05°. However, spectrums include the data between 10-60 ^{o} for MoO_x samples and

24

between 30-40$^{\mathrm{o}}$ for Zn$_x$Mg$_{1-x}$O samples in order to focus only on signals coming from the samples.

2.3. X-ray Photoelectron Spectroscopy (XPS)

Working principle of XPS is based on Einstein's Nobel Prize winning theory "photoelectric effect" which had been observed by Heinrich Rudolf Hertz but could not be explained at that time. The theory tells that when a material is objected to light, it produces electron or free charge carriers. In the case of XPS measurement, the photon is X-ray which is shone onto material.

XPS is a surface sensitive and quantitative elemental composition analysis. Also, it is capable of determining valance band, work function and defect bands in the band gap of a material. It gets signal from outer surface of a material within approximately 10 nm depth. When electrons in a core level are ejected, they leave empty spaces to be occupied by electrons which are lying on a lower energy levels [25]. For energy conservation, there should be another electron ejected which is Auger electron as illustrated in Figure 2.8.
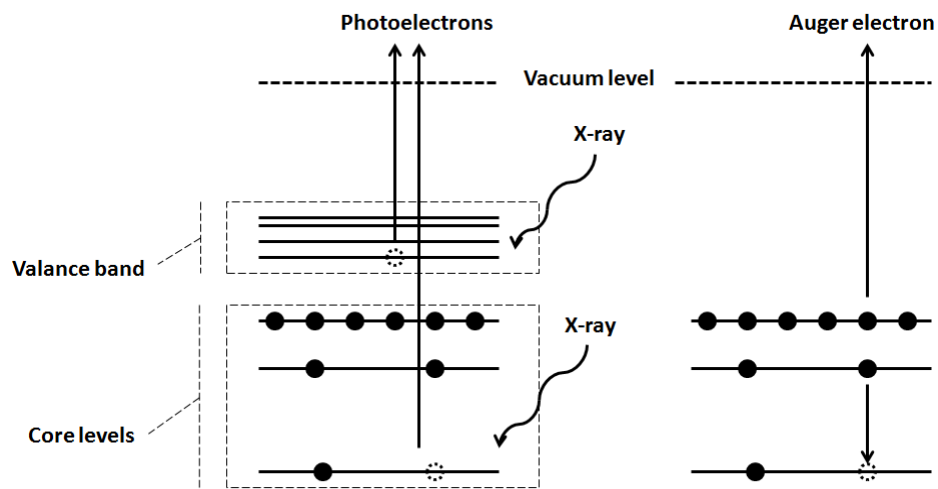
Figure 2.8. Schematics of X-ray and Auger photoelectron spectroscopy

25

In order to perform XPS measurement, X-ray with energy hν is sent to the sample and ejected electrons reach to detector with a kinetic energy, KE. Binding energy of electrons ejected from material was found by the following equation;

$$E_{\text{Binding energy}} = h\nu - KE_{\text{electron}} + \phi, \qquad \text{(Eq. 2.12)}$$

where ϕ is work function both material and spectrometer dependent, which is an adjustable instrumental correction factor. It is absorbed by detector and needs to be adjusted for each instrument in practice.
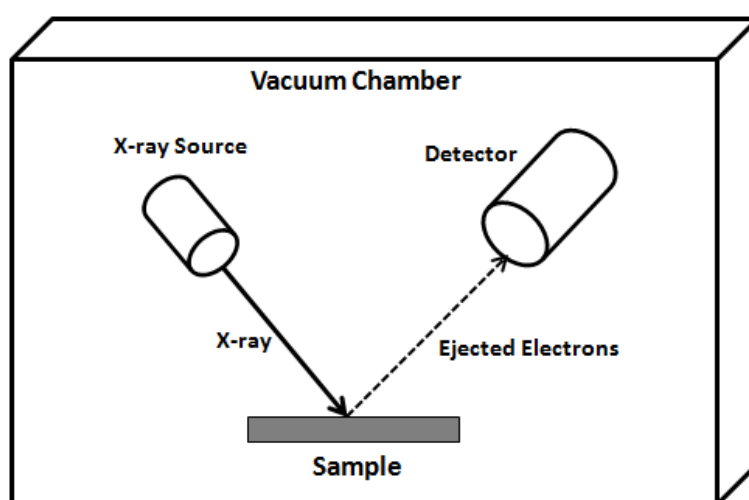
Figure 2.9. Schematics of X-ray photoelectron spectroscopy (XPS) instrument

XPS measurements in this study were performed in the METU Central Laboratory using PHI VersaProbe XPS system. Each measurement were carried out with dwell time of 200 ms and step of 0.1 eV.

CHAPTER 3

MoO$_x$ AS HTL AND Zn$_x$Mg$_{1-x}$ AS ETL

Transition metal oxides such as ZnO$_x$, MoO$_x$, TiO$_x$ and NiO$_x$ are commonly used as charge transport layers in heterojunction solar cells [26][27][28][11].

Transition metals have partially filled d-orbitals in the penultimate shell which is located right before the outer shell. Incomplete penultimate orbitals give these elements very distinctive properties. First of all, they have very dense structures resulting in a strong hardness, and high boiling and melting points. Secondly, unpaired electrons in those materials create paramagnetic properties since they induce magnetic moment in the host atom making it acts like a magnet. In the presence of an external magnetic field, these randomly oriented small magnets are oriented in the same direction and the lines of force are drawn through the substance. Lastly, most of the transition metals with some exceptions such as Sc, Y, and Zn may possess variety of oxidation states. It relies on the fact that both outer shell and penultimate shell electrons may be used in bonding due to very small energy difference between them. The ability of transition metals to change their oxidation states enables them to be used as catalysts. Moreover, material properties of transition metal oxides can be tuned by forming different oxidation states of transition metals. Different electronic phases, multiple bonding forms and ability of transition metal to exchange their charges with other ions such as oxygen are all resulted from electron-electron interactions in partially filled d- shells of ions [29]. In bulk transition metal oxides, 2p-orbitals of oxygen atoms overlap and come up with

lower energy of highly populated valance band while d-orbitals of transition metals overlap and form conduction band of material [30].

Transition metal oxides typically possess defect sites due to oxygen vacancy or cation vacancy. Defects can be created by post treatments such as high temperature, energetic electron bombardment and UV-O_3 treatment, and they significantly alter electronic energy levels of materials [67].

3.1. Literature Survey for MoO$_x$ as HTL

Hole transport layer (HTL) is in charge of transporting photogenerated holes to positive electrode in a heterojunction solar cell. In this regard, conventional HTL is supposed to possess high electrical conductivity, high work function and defect-free interface with electrode and absorber material. Also, they have to be transparent if they are adjacent to the front contact which meets sunlight before the absorber layer. Researchers work on various HTL materials that can be utilized in heterojunction structures. In order to provide those solar cells with the most efficient hole transport characteristic, they alter material stoichiometry during deposition, and then, they either treat fabricated materials with a post annealing step at different ambient, or UV-O_3 exposure, or they dope the materials with different dopants. Additionally, different hole transport materials can be stacked on top of each other to enhance the overall structure in terms of conductivity, transparency, band alignment and stability.

Among the common hole transport layers, MoO$_x$ is one of the promising candidates for heterojunction solar cells due to its stability and controllable high work function [31]. Molybdenum, with its 42 protons and 54 neutrons, is a transition metal which constitutes the 5th row of group 6 elements in the periodic table and has the ground state configuration, [Kr] d^{5}s^1. Mo possesses electrical and thermal conductivity. Unlike most of the metals, molybdenum can easily be etched by oxidizing agents such as Na_2O_2, $KClO_3$ and KNO_3 yet, interestingly, it cannot be etched with HF, HCl or H_2S.

28

Stoichiometric MoO_3 is a semiconductor with approximately 3.3 eV band gap where its valance band is determined by O 2p orbital. It has such a high work function that Fermi level can be even located below the valance band of some absorber materials such as perovskite. However, oxygen vacancy formation in the MoO_x crystal enables it to shift its Fermi level and to lower the work function [32]. In a heterojunction structure, Fermi level of MoO_x has to be right above valance band of absorber material to be effectively used as hole selective layer.

With the creation of oxygen vacancy in MoO_3, both the band gap and work function decrease. Also, the tail of the defect band brings about formation of low density of defect states in Fermi level. If molybdenum ions in the oxide are reduced to Mo^{4+}, MoO_2 is considered as a high work function metal due to electron occupancy in conduction band which is formed by molybdenum $d_{3/2}$ and $d_{5/2}$ orbitals as seen Figure 3.1. Shortly, controllable defect state formation within the band gap enables to achieve optimum work function value for MoO_x with respect to the adjacent materials. In 2014, Corsin et al. reported the defect state formation and the shift of the Fermi level of MoO_x by UV-O_3 treatment and post annealing [26]. Zheng Zhang et al. also studied the effect of oxygen vacancy on energy band alignment at MoO_x/organic interfaces. They revealed the oxygen vacancy formation with increasing RTA annealing temperature and reduced work function [33].
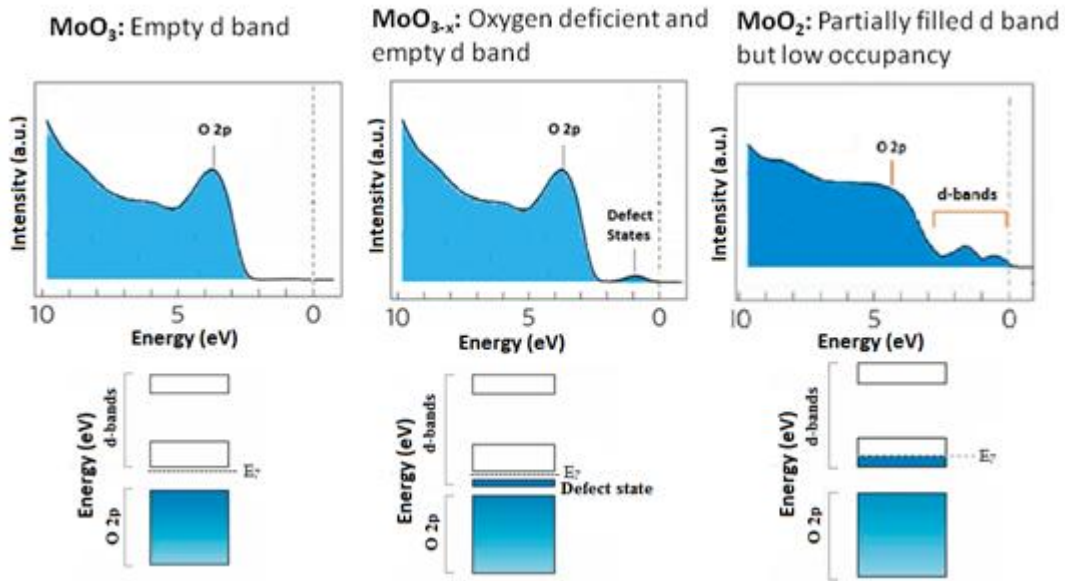
Figure 3.1. The figures on top illustrate valance photoemission spectra of MoO_3 with empty d band, O_2 deficient MoO_x with empty d band and MoO_2 with partially filled d band, respectively; the figures below are schematics electron band diagrams [32].

MoO_x with oxygen vacancies acts like degenerate n-type material. MoO_x Fermi level shifts towards the edge of conduction band or above it depending on free electron concentration. F. Xie and W. C. H. Choy studied the effect of oxygen vacancy on electronic properties of MoO_x. The band diagrams of MoO_x thin films with oxygen vacancies (on the left) and excess oxygen (on the right) is given in Figure 3.2 [34].
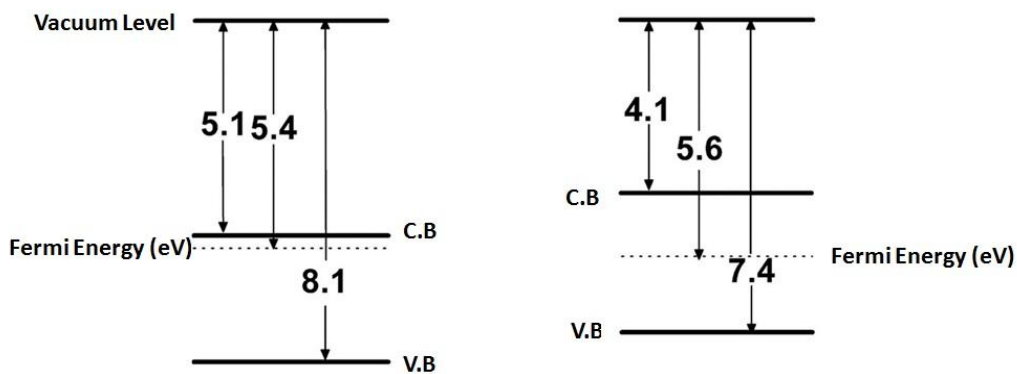
Figure 3.2. Energy band diagram of MoO_x with oxygen vacancy (on the left) and with oxygen excess (on the right) [34].

MoO_x is capable of conducting holes to adjacent materials which have relatively lower work function such as ITO as illustrated in Figure 3.3. Therefore, MoO_x plays the role of hole extraction when it is in contact with various absorber semiconductor materials [35].
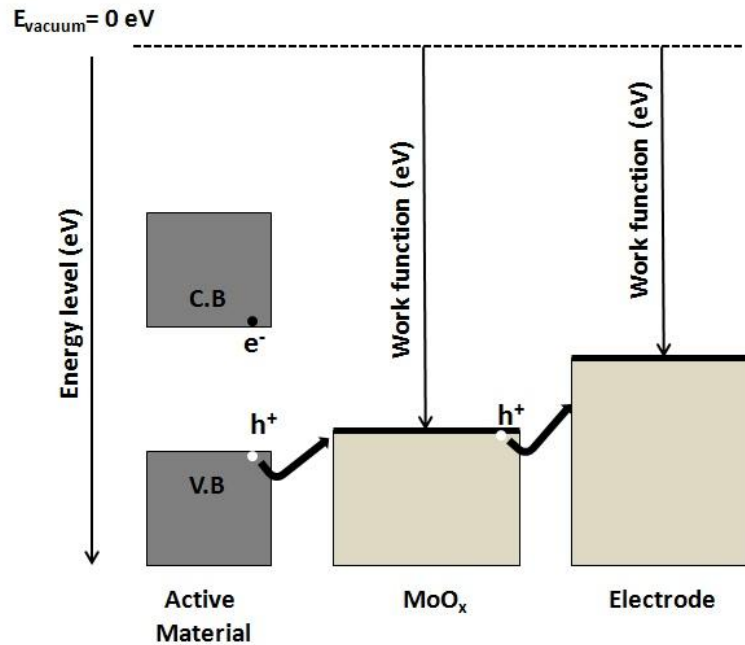
Figure 3.3. Hole transport mechanism through n-type MoO_x hole transport layer

Apart from optical and electrical issues, one should also consider the compatibility of hole transport layers with adjacent materials. In this context, variety of materials has been covered in the literature. For instance, PEDOT:PSS is the most commonly used HTL owing to its high electrical conductivity; however, it causes the perovskite layer to decompose and it etches the ITO layer. Therefore, MoO_x can be used as an alternative HTL material which is a friendlier material for ITO and perovskite compound although it has a weaker coverage of perovskite.

Malhotra and Lalit conducted a study on MoO_x and PEDOT:PSS deposited on organic solar cells. Their aim was to compare two competitive hole transport materials in terms of efficiency and stability perspective. They fabricated optimized MoO_x and PEDOT:PSS on organic cells and observed their PCEs. The cell structure was constructed on an ITO coated glass substrate. They first deposited 50 nm of

PEDOT:PSS and 5-6 nm of MoO_3 as HTL on top of the same quality of ITOs. They concluded that the organic solar cell constructed on MoO_3 HTL gives a better PCE and provides a longer term stability [36].

Another study regarding the comparison of PEDOT:PSS, MoO_3 and composite MoO_3-PEDOT:PSS hole transport layers by Shuyan *et. al.* was reported in 2013. They comprehensively examined the PCE values of polymer bulk heterojunction (BHJ) solar cells fabricated with MoO_3, PEDOT:PSS and composite MoO_3-PEDOT:PSS hole transport layers. They stated that the highest efficiency was obtained as 6.4% from BHJ solar cell with 10 nm thick composite MoO_3-PEDOT:PSS hole transport layer. The PCE of the solar cells with 50 nm PEDOT:PSS and 10 nm MoO_3 HTL were 5.5 and 5.4%, respectively. Moreover, the stability problem of the cell with PEDOT:PSS was inevitable. The PCE of the cell with PEDOT:PSS HTL, which was stored in dark, decreased to zero in 10 days but the one with MoO_3 was still above 50% of its initial performance. The one with composite MoO_3-PEDOT:PSS HTL had the highest life time in terms of stability [37].

The stability and PCE improvement of HTL by MoO_x doping was also demonstrated by Liu *et al.*. They achieved to dope TiO_2/MoO_3 core/shell nanoparticles with the size of 40 nm into PEDOT:PSS hole transport layer which was fabricated for perovskite solar cell. According to their results, PCE has been improved 31% with incorporation of TiO_2/MoO_3 core/shell nanoparticles in PEDOT:PSS HTL. Moreover, the storage time extended enormously. The efficiency of the perovskite with PEDOT:PSS decreased from approximately 9 % to less than 2% in 400 hours; however, it decreased from approximately 12% to 10% in the same storage time after doping PEDOT:PSS by TiO_2/MoO_3 core/shell nanoparticles [38].

Hou F. *et al.* deposited MoO_3 with different thicknesses ranging from 4.2 to 38.6 nm between ITO and PEDOT:PSS by milder thermal decomposition solution method and achieved a PCE increase of 30% after insertion of MoO_3/PEDT:PSS bilayer with an optimum thickness between PEDOT:PSS and ITO in inverted perovskite structure. Also, stability of the device was improved [39].

A study on determination of optical constants (refractive index and extinction coefficient) of MoO_x was reported by Szekeres *et.al.* in 2002. They measured refractive indices (n) of the samples grown by chemical vapor deposition (CVD) between 1.8 and 2.2 in the visible range. Moreover, extinction coefficients (k) of them varied around 0.2 [40].

3.2. Literature Survey for $Zn_xMg_{1-x}O$ as ETL

Electron transport layer (ETL) is used to transport photogenerated electrons from absorber layer to the negative electrode in a heterojunction solar cell. The conduction band of ETL has to be aligned with that of the absorber layer for an efficient electron extraction as illustrated in Figure 3.4. Small offset between the conduction band energies of ETL and absorber layer is to provide some momentum to electron and also to limit electrons to diffuse back to the absorber layer.
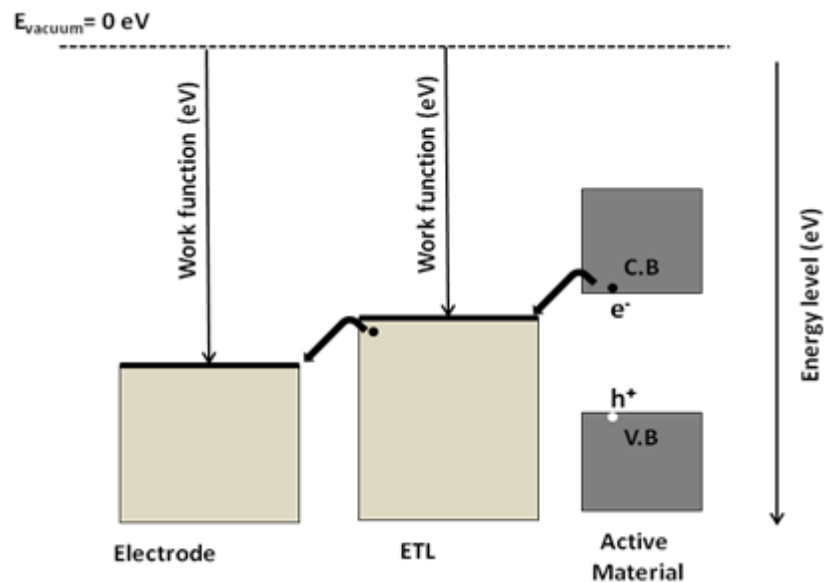
Figure 3.4. Electron transport mechanism through an electron transport layer

Organic materials such as PCBM and P3HT as well as inorganic materials such as TiO_2, SnO_2, ZnO and their doped and alloyed forms are typically utilized as ETL. Spin coating and spray pyrolysis are common techniques to fabricate ETL materials.

However, physical methods such as atomic layer deposition (ALD) and sputtering are known to allow dense and uniform layers with superior surface coverage.

Among many alternative ETL materials, ZnO_x is one of the promising candidates due to its low cost and high electron conductivity [41]. Zinc has ground state electron configuration of $[Ar]3d^{10}4s^2$ and exhibits only one oxidation state (+2). When zinc makes an ionic bond with oxygen, it gives two electrons of outer 4s orbital to oxygen and ends up with empty 4s level. Oxygen, on the other hand, ends up with filled 2p level. When molecules come together to form bulk materials, these energy levels creates band formation. According to cellular and the tight binding methods, 4s band of zinc overlaps 3d band in the oxide form and results in broadening of band width in XPS. While 3d band can be occupied by 10 electrons, 4s can hold 2 electrons per atom. [42].

Zinc oxide (ZnO_x) can be found in three possible crystal structures which are hexagonal wurtzite, cubic zincblende and rock salt. At ambient pressure and air, it intends to crystallize in the wurtzite structure, in which Zn ions are surrounded by tetrahedral of O ions as seen in Figure 3.5. On the other hand, stable zincblende ZnO can only be grown on a cubic structure substrate while rock salt is metastable phase forming at very high pressure of approximately 10GPa [43].

(a)   (b)   (c)
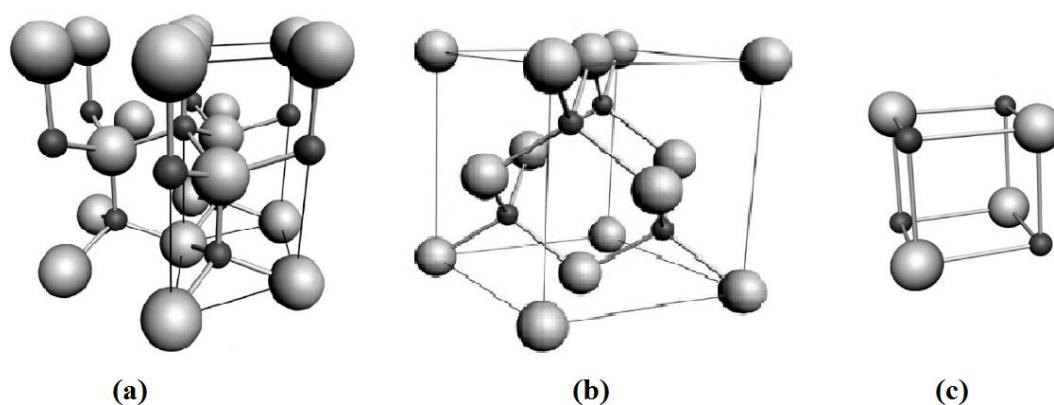
Figure 3.5. The hexagonal wurtzite (a), zincblende (b) rock salt (c) phases of ZnO. Zn atoms are shown as small black and O atoms are large white spheres [43].

Zinc oxide (ZnO_x) with hexagonal wurtzite structure has a direct band gap around 3.4 eV [43][44]. The lowest level of conduction band and the highest level of valence band of ZnO with respect to the vacuum level are around -4.4 eV and -7.8 eV, respectively. ZnO_x blocks UV light since it has band edge cut-off at around 375 nm. This can be also an advantageous in terms of stability of absorber layer in organic and perovskite solar cells [44]. Additionally, the refractive index of wurtzite ZnO is calculated between 2.002 an 2.029 [45].

As in the case of most wide band gap semiconductors, p-type doping of ZnO is not easy to attain. It is inherently prone to behave as n-type material due to formation of oxygen vacancy sites. Native defects such as O vacancies and Zn interstitials are thought to obstruct p-type doping of ZnO [46].

There are controversial arguments on controlling the conductivity of ZnO_x which has an unintentional n-type conductivity which is typically assumed to be due to oxygen vacancies [47][48][49]. However, Van de Walle claimed that unintentional n-type conductivity of ZnO_x has nothing to do with oxygen vacancy or Zn interstitial but it does with unintentional incorporation of impurities such as hydrogen, which acts like shallow donors [50]. According to their density functional calculations, oxygen defects are deep donor and cannot make any contribution to being n-type conductivity. They claimed that interstitial H forms a strong bond with oxygen in ZnO_x. However, experimental proof of H dependence of conductivity was not satisfied due to high mobility of interstitial H through the material [51][52]. Even at low annealing temperatures, hydrogen easily diffuses out of ZnO_x and causes an unstable conductivity that restricts observation of the influence of H on conductivity.

ZnO_x has been commonly used in perovskite, CdTe, CIGS, Cu_2O and organic solar cells [53][44][54][55][56]. The overall performance of solar cells strongly depend on optimization of ZnO_x layer.

According to a study conducted by S.Lattante, P3HT:PCBM-based solar cell spans from 2% to 4% efficiency depending on the optimization of ZnO_x layer [57]. One of the most important optimization parameters is the roughness of the ZnO_x layer. Yu *et al*. studied the effect of annealing rate on light trapping of sol-gel derived ZnO

incorporated to P3HT:PCBM-based inverted solar cell. They controlled the surface roughness by simply changing the post annealing temperature rates of ZnO_x layer fabricated by sol-gel method. They observed an increase in PCE from 2.08% to 2.88% with lowering the temperature increase rate to $9^oC/min$ during annealing and related it to better crystallization and enhanced absorption of rougher ZnO_x surface [58]. Elumalai *et al.* also studied the effect of post annealing of ZnO layer which was employed as ETL within the device configuration ITO/ZnO/P3HT:PCBM/MoO$_3$/Ag. They concluded that the device incorporating ZnO annealed at 240 ^oC showed 40% higher PCE than the one with ZnO annealed at 160 ^oC. Besides, the one with ZnO annealed at 240 ^oC showed longer stability. They claimed that the improvement in PCE was resulted from decrease in the density of localized energy states in the band gap of ZnO due to enhanced crystallinity[59].

Thickness is another optimization parameter of ZnO_x ETL. Hu *et al.* showed that the work function and surface morphology of ITO/i-ZnO depended on thickness of ZnO layer. Among the P3HT:PCBM based solar cells incorporating ZnO with various thicknesses, the one with 80 nm thick ZnO performed the best PCE of 2.93% [60]. H.Cheun *et al*. also investigated the performance of the inverted polymer solar cell with various ZnO thicknesses. They claimed that the performance of the device was degraded when the thickness of ZnO was to less than 10 nm. They also claimed that they enhanced the performance by UV exposure onto ZnO to increase the oxygen desorption and consequently conductivity [53].

Stoichiometry is also studied for optimization of ZnO layer as ETL. Tseng *et al.* investigated the influence of stoichiometry of 40 nm thick ZnO_x on PCE of perovskite solar cells with device architecture ITO/ZnO/CH$_3$NH$_3$PbI$_3$/spiro-OMeTAD/Ag. The highest efficiency, 15.9%, was obtained from the perovskite solar cell incorporating ZnO_x layer which was fabricated by magnetron sputtering. The efficiency of the device with ZnO which was fabricated with additional oxygen flow was 12.4%. They stated that the high performance of device with ZnO fabricated without additional O may be due to higher conductivity, or better interface contact with perovskite, or better match of energy levels of their frontier orbitals [61].

Tuning the energy band gap is also studied in the scope of optimization of ZnO layer by doping with various materials such as magnesium and cadmium. While the band gap of undoped ZnO is around 3.37 eV, it can be increased by Mg or decreased by Cd incorporation. In a study, Sanjeev $et\ al.$ synthesized Mg doped ZnO_x samples by sol-gel method. The samples were doped with different Mg ratios between 0 to 5%. They reported that optical band gap of ZnO was measured as 3.1, 3.32 and 3.36 eV for 0%, 2% and 5% Mg doped ZnO_x samples, respectively [62].

Lastly, it is worth mentioning the electron transport bilayer with two different materials stacked on top of each other which combines the advantages of lower interfacial recombination and higher electron extraction. The perovskite cell configuration with FTO/ZnO(50nm)/perovskite/Spiro-OMetaD/Au fabricated by Xu X. $et\ al$. achieved 16.1% efficiency. When 10 nm thick TiO_2 was inserted between FTO and ZnO, the efficiency increased to 17% due to enhanced FF and V_{oc} values [63].

CHAPTER 4

FABRICATION AND CHARACTERIZATION OF HTL AND ETL

This chapter was divided into two parts. In section 4.1, we will discuss MoO_x samples fabricated with different stoichiometry by both reactive DC and RF sputtering methods. The samples fabricated by reactive RF sputtering were analyzed to investigate the effect of stoichiometry on their work function by XPS. Then, they were exposed to UV-O_3, rapid thermal annealing (RTA) under nitrogen flow and hot plate annealing in ambient air. The work functions of those samples were also measured by XPS. Furthermore, optical and crystallographic analyses of the samples were performed.

In section 4.2, experimental studies of $Zn_xMg_{1-x}O$ films fabricated by co-sputtering and reactive co-sputtering were covered. Fabricated samples were analyzed by optical and structural characterization techniques. Finally, ZnO_x was utilized in perovskite solar cell.

Before fabrication of thin films, the substrates were cleaned with acetone, isopropanol alcohol (IPA), hydrofluoric acid (HF) (only for silicon) and deionized (DI) water. In the last step, they were dried up with nitrogen gun. In all depositions base pressure in the chamber was less than $7x10^{-7}$ Torr.

4.1. MoO$_x$ as HTL

MoO$_x$ thin films were fabricated by reactive DC and RF sputtering techniques. It should be noted that RF sputtering is superior in sputtering of insulator targets. Although Mo metallic target has been used in the fabrication of the thin films, it is unavoidable to form a MoO$_3$ layer on the target surface when high oxygen flow rates are applied. Therefore, in this thesis research we used the samples fabricated by reactive RF sputtering in characterization studies.

4.1.1. MoO$_x$ by Reactive DC Sputtering

The power applied to the Mo target was set at 50 Watt, and oxygen flow rate was altered to vary the stoichiometry of the films. Depositions were carried out under 8 mTorr pressure for 15 minutes. Deposition parameters of MoO$_x$ samples fabricated by DC reactive sputtering are given in Table 4.1.

Table 4.1. Deposition parameters of MoO$_x$ films fabricated by DC reactive sputtering

Sample Name	Oxygen Flow (sccm)	Argon Flow (sccm)	Thickness measured by ellispmeter (nm)
DC0.9_MoO$_x$	0.9	19.1	65.7
DC1.0_MoO$_x$	1	19	61.9
DC1.1_MoO$_x$	1.1	18.9	56.5
DC1.2_MoO$_x$	1.2	18.8	55.3
DC1.3_MoO$_x$	1.3	18.7	52.5
DC1.4_MoO$_x$	1.4	18.6	49.3
DC1.5_MoO$_x$	1.5	18.5	40.6

MoO$_x$ films were characterized by spectroscopic ellipsometry to determine their optical constants and thicknesses. In this study, Δ and Ψ values measured by spectroscopic ellipsometry were fitted using Cauchy equation in the range of 1.23-3 eV photon energy. We found that both refractive index and extinction coefficient of MoO$_x$ films decrease with increasing oxygen flow rate as shown in Figure 4.1. The

change of refractive index with O_2 gas flow points out that the stoichiometry can be controlled sensitively by reactive DC sputtering.
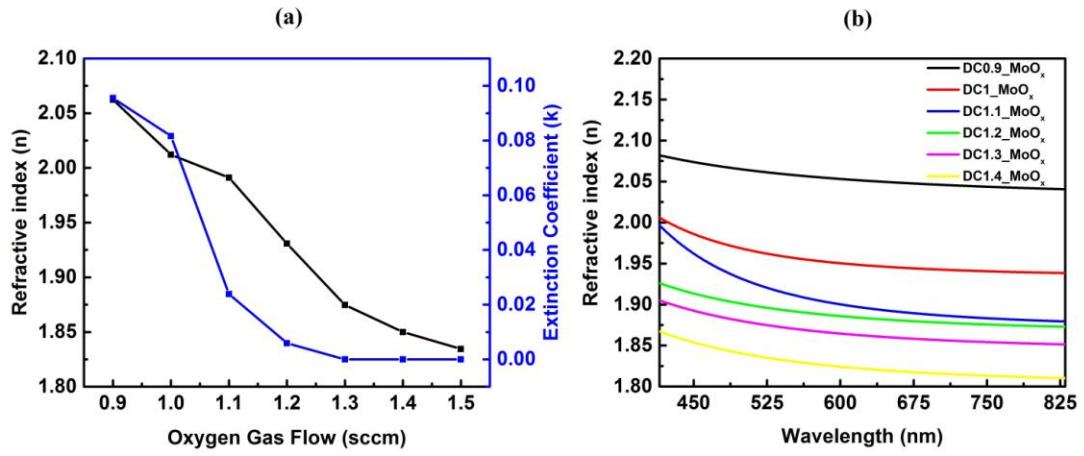
Figure 4.1. (a) Refractive indices of MoO_x by reactive DC sputtering versus wavelength (b) The change of optical constants of MoO_x films fabricated by DC sputtering with O_2 gas flow

4.1.2. MoO_x by Reactive RF Sputtering

Two MoO_x with different Mo/O_2 ratios were fabricated by reactive RF sputtering technique. Power of Mo target was set at 150 Watt, and O_2 flow rate was set at 1.5 and 2 sccm to achieve two different stoichiometries; one being near stoichiometric MoO_3 and another one is Mo-rich MoO_x. Both of the depositions were carried out under 4 mTorr for 50 minutes to achieve similar thicknesses for both films. Deposition parameters are given in Table 4.2.

Table 4.2. Deposition parameters of MoO_x fabricated by reactive RF sputtering and thickness values of films measured by spectroscopic ellipsometry

Sample Name	O_2 flow rate	Ar flow rate	Thickness
Mo-rich MoO_x	1.5 sccm	18.5 sccm	106.5 nm
Near Stoichiometric MoO_3	2 sccm	18 sccm	111.7 nm

41

For optical constant and thickness analyses on ellipsometry measurement of MoO_x thin films fabricated on silicon wafers, Cauchy model was used in the range of 1.23 and 2.5 eV. Refractive indices and extinction coefficients of the samples decrease with increasing oxygen flow rate as shown in Figure 4.2. Refractive indices and extinction coefficients values are consistent with the ones fabricated by reactive DC sputtering with similar stoichiometries.
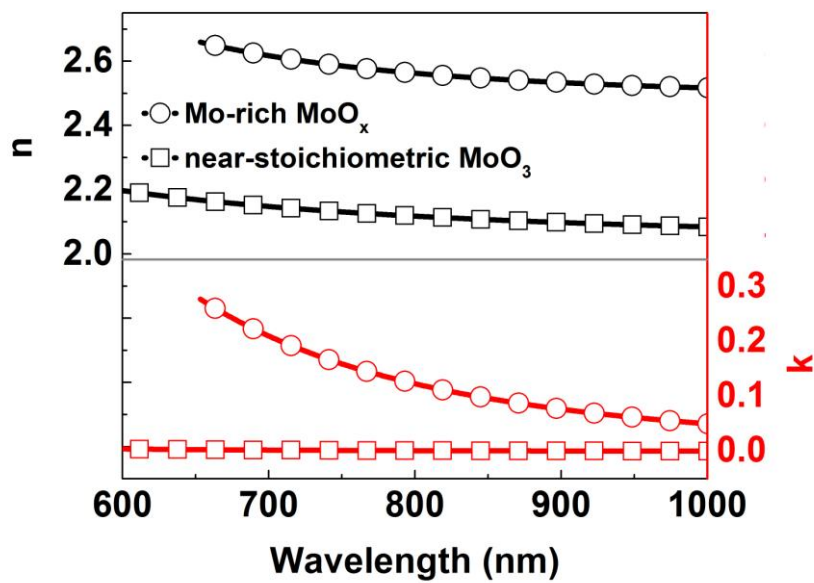
Figure 4.2. Optical constants versus wavelength plot of MoO_x samples fabricated by reactive RF sputtering

Mo-rich sample has a stronger absorbance in the visible spectrum due to interband states caused by lower oxidation states (Mo^{4+} and Mo^{5+}) of Mo. Mo-rich MoO_x sample has also a slightly smaller optical band gap as illustrated in Figure 4.3.
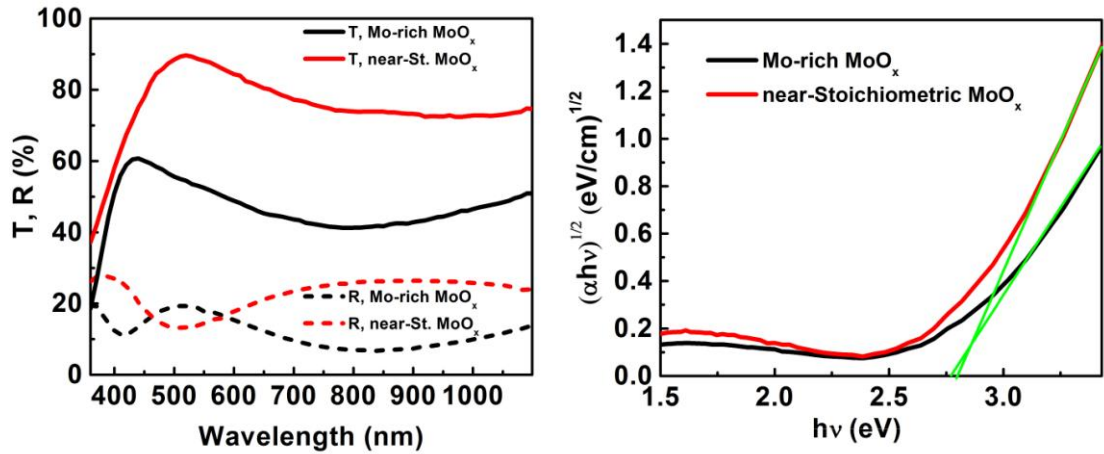
Figure 4.3. Transmittance and reflectance spectra (left), and Tauc plot (right) for MoO_x thin films fabricated by reactive RF sputtering

Molybdenum ions in MoO_3 with filled $3d_{3/2}$ and $3d_{5/2}$ doublet orbitals has oxidation state, +6. When Mo^{6+} is reduced to Mo^{5+} or lower oxidation states, defect states in the band gap provide MoO_x with n-type characteristics by shifting Fermi level towards the CB. As a result, it can be deduced that the more oxygen defect sites, the smaller work function and band gap of MoO_x [34]. In this study, we found that the work function of Mo-rich MoO_x sample as 5.1 eV while that of near stoichiometric MoO_x as 5.25 eV as shown in Figure 4.4.
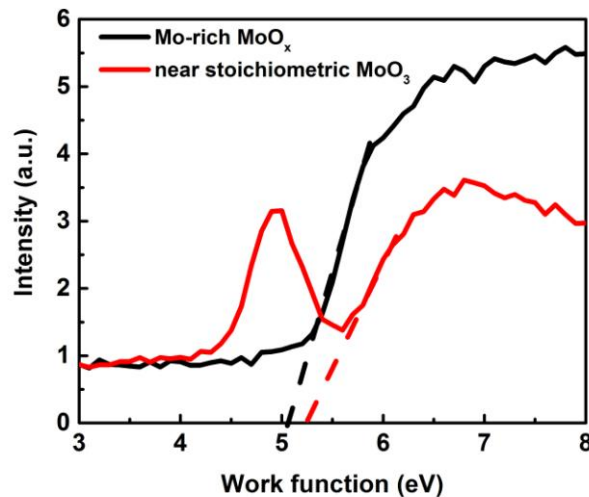
Figure 4.4. XPS spectrum of MoO_x thin films by reactive RF sputtering with different O_2/Ar gas flow ratios. Dotted line is the linear fit to data. Its value at the noise level provides the work function of the films.

We also showed that the density of defect states in the band gap of MoO_x can be altered by N_2 annealing. The near-stoichiometric MoO_x sample was annealed at 300, 400 and 500 ^oC under nitrogen flow to inhibit oxygen in the ambient. XPS results show a slight shift for the defect state energy towards the Fermi level as shown in Figure 4.5. Additionally, the intensity of the peak related with the defect states increases with annealing except the sample annealed at 500 ^oC. The density of defect states seems to be relatively lower than the one annealed at 400 ^oC which can be due to enhanced diffusion of ions helping to reduce the defect state density at high temperature treatment. Additionally, we showed that the work function decreases with annealing temperature as shown in Figure 4.5 [33].
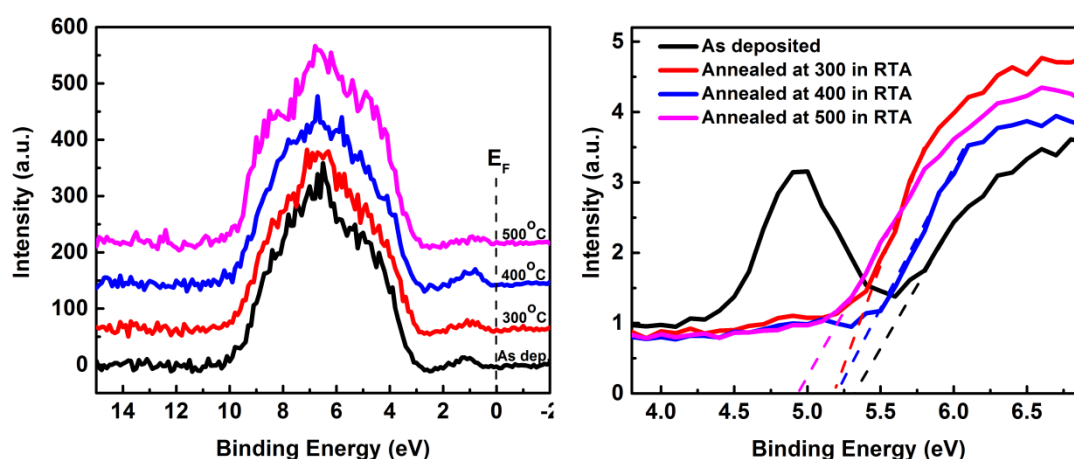
Figure 4.5. XPS spectrum of the near stoichiometric MoO_x sample annealed under N_2 flow in RTA showing density of states in the valence band and near the Fermi level (left) and fits to obtain the corresponding work function values (right)

Effect of hot plate annealing in ambient air was also studied for the near stoichiometric MoO_x sample. Defect state formation and the corresponding work function of the material is not very controllable in this case as seen in Figure 4.6. since oxygen vacancy formation is irreversible. In other words, both reduction and oxidation of molybdenum ion take place depending on the temperature and the oxygen amount in the ambient. If the sample had been annealed under oxygen flow, each molybdenum ions would have turned out to be Mo^{6+}[26]. In this case, annealing

was conducted in ambient air, and it is difficult to interpret the oxidation-reduction mechanism.

Defect states gradually disappeared with increasing hot plate annealing temperature. However, they came up and shifted towards the Fermi level when the sample was annealed at 400°C. It implies that molybdenum ions were reduced to lower oxidation states at this temperature. This is also consistent with the work function measurements performed by XPS. The reason of reduction of Mo ions at 400 $^{\circ}$C hot plate annealing will be investigated deeply.

As a result, one should consider uncontrollable slight shifting in the work function of MoO_x in case of hot plate annealing especially above 200 $^{\circ}$C. However, if band alignment with adjacent materials are provided, decrease in defect states can be an advantage in case of reduction of recombination, too
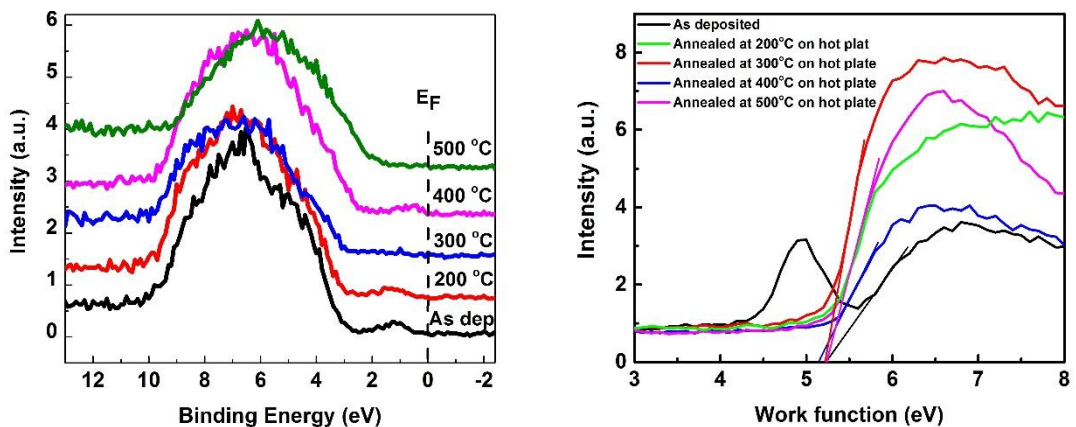
Figure 4.6. XPS spectrum of the near stoichiometric MoO_x sample annealed in ambient air on a hot plate showing density of states in the valence band and near the Fermi level (left) and fits to obtain the corresponding work function values (right)

Transmittance and reflectance of each sample, which were annealed at 300, 400 and 500 $^{\circ}$C on hot plate in ambient air for 1 hour, were also analyzed. Transmittance of Mo-rich MoO_x sample was enhanced very rapidly after annealing at 300 $^{\circ}$C due to the crystallization of the material as seen in Figure 4.7. Also, oxidation of interstitial molybdenum ions to higher states with oxygen in the air may have been effective on enhancement of transmittance.

45
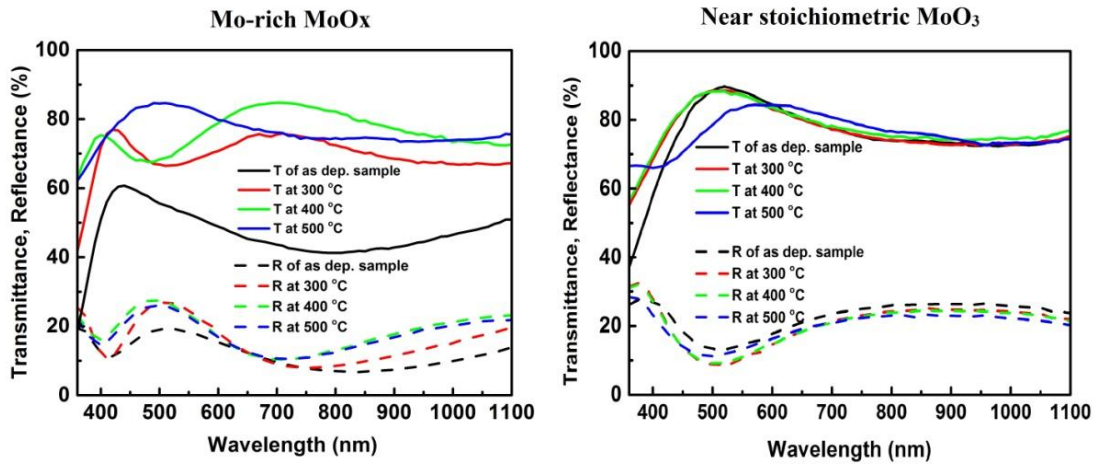
Figure 4.7. Transmittance and reflectance of MoO$_x$ samples annealed on hotplate in ambient air

Finally, we exposed the Mo-rich MoO$_x$ thin film to UV/O$_3$ plasma for 30 minutes. The work function increased approximately 0.1 eV after UV/O$_3$ treatment as seen in Figure 4.8. According to Corsin *et al*., increase in work function results from the removal of adventitious carbon at the surface [26].
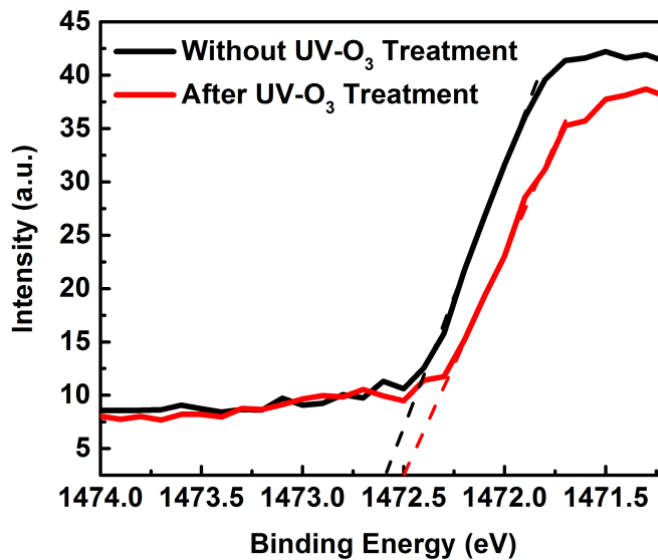
Figure 4.8. The effect of UV-O$_3$ treatment on work function of MoO$_x$.

XRD measurement were carried out to investigate the crystallization of the samples deposited on glass and silicon substrates. The ones deposited on glass substrates have

single phase after annealing at 300 ^{o}C regardless of their stoichiometries. On the other hand, phase formation of the samples on silicon substrates are temperature and stoichiometry dependent. Although Mo-rich MoO_x sample has a single phase regardless of annealing temperature, it was not the case for the near stoichiometric MoO_3 sample. For the near stoichiometric MoO_3 sample on silicon wafer, different phase formations occur at different annealing temperatures. Nevertheless, they all turn out to be single phase when annealed at 500 ^{o}C as seen in Figure 4.9.
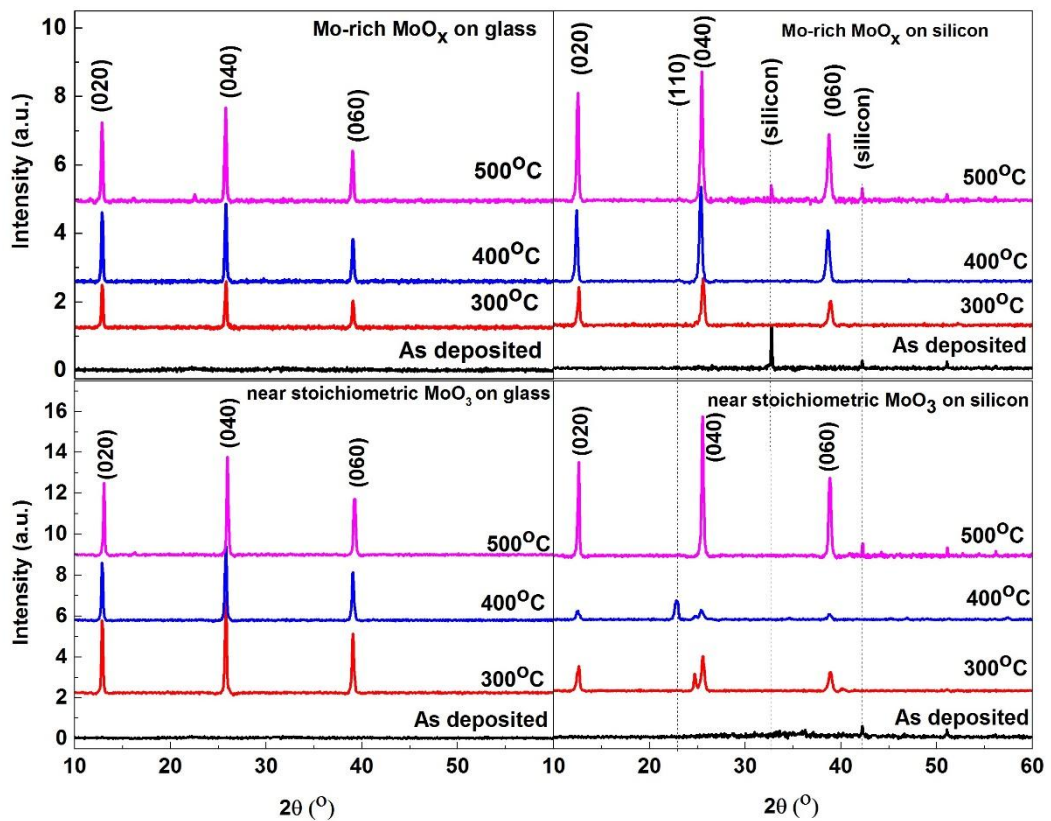
Figure 4.9. XRD spectrum of the MoO_x samples fabricated on glass and silicon substrates

4.2. $Zn_xMg_{1-x}O$ As ETL

Three sets of ZnO_x samples were fabricated and investigated. These sets are

- ZnO_x films doped with various concentrations of Mg,

47

- ZnO$_x$ films sputtered at various O$_2$ flow rates,
- ZnO$_x$ films were fabricated with different thicknesses.

Fabricated films were investigated by means of crystal structure (using XRD) and optical analyses (using ellipsometry, and transmission and reflection measurements).

4.2.1. Magnesium Doped Zinc Oxide (Zn$_x$Mg$_{1-x}$O)

Zn$_x$Mg$_{1-x}$O samples were fabricated at different Mg concentrations by co-sputtering to observe Mg doping effect on optical, electrical and structural properties of ZnO$_x$ thin film. Concentration was altered by changing DC power applied to Mg target. All samples were fabricated at 4 mTorr pressure and the power of ZnO$_x$ target was set at 300 Watts. Deposition parameters and the thicknesses of the samples measured by ellipsometry are given in Table 4.3. During sputtering of ZnO$_x$_150Mg sample, additional O$_2$ was introduced to the chamber to avoid excessive interstitial Zn and Mg atoms.

Table 4.3. Deposition parameters of Zn$_x$Mg$_{1-x}$O samples

Sample Name	RF Power of ZnO (Watt)	DC Power of Mg (Watt)	Ar Flow (sccm)	O$_2$ Flow (sccm)	Deposition Time (min)	Thinkness (nm)
ZnO$_x$	300	-	20	-	45	428.4
ZnO$_x$_20Mg	300	20	20	-	45	361.463
ZnO$_x$_40Mg	300	40	20	-	45	402.563
ZnO$_x$_150Mg	300	150	19	1	14	105

Refractive index versus wavelength graphs were plotted for the samples fabricated using the same parameters except Mg ratio. A decrease in the refractive index of the material with increasing Mg concentration throughout the visible wavelengths as seen in Figure 4.10 (left). According to the UV/Vis. measurements, the ZnO$_x$ thin film with the higher Mg doping level has higher transmittance in the near UV spectrum as shown in Figure 4.10 (right). Additionally, constructive and destructive interferences are formed in all samples.
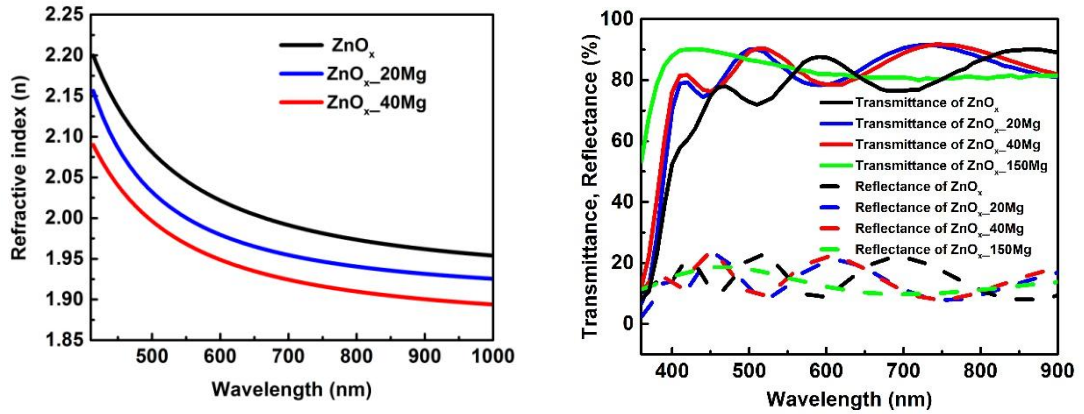
Figure 4.10. Refractive index spectra (left), and transmittance and reflectance spectra of as deposited $Zn_xMg_{1-x}O$ samples (right)

Optical band gap values of the samples obtained from Tauc analyses increase with Mg/Zn ratio as expected [64]. Stoichiometric ZnO is supposed to have band gap of 3.3 eV. However, ZnO_x naturally tends to have oxygen defect sites, which reduces its band gap by band tail formation. We measured the optical band gap of the ZnO_x thin film as approximately 3.16 eV. Optical band gap of $Zn_xMg_{1-x}O$ increases gradually with Mg concentration. We obtained an optical band gap value of approximately 3.34 eV at the highest Mg/Zn ratio.
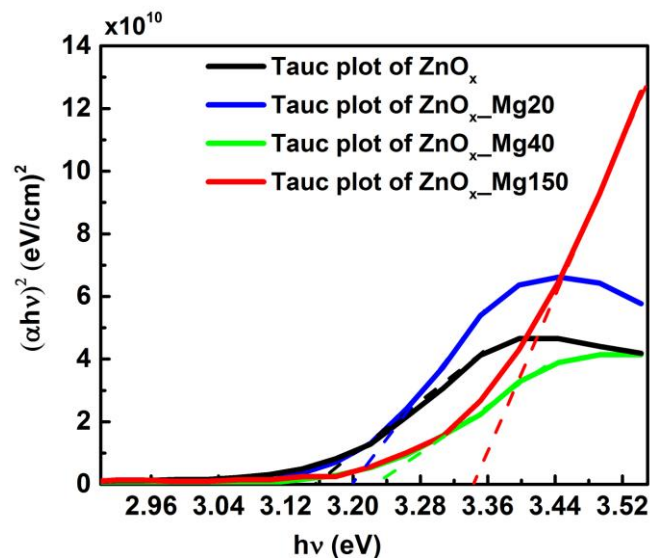
Figure 4.11. Tauc plot for $Zn_xMg_{1-x}O$ films indicating band gap tuning with Mg/Zn ratio

According to XRD analysis, ZnO_x is in hexagonal wurtzite phase for all Mg concentrations. However, co-sputtering of ZnO_x with Mg deteriorated the crystal structure of ZnO_x, which resulted in a broadening of bandwidth. Moreover, MgO peak appears at relatively high Mg/Zn ratio.

We also observed an enhanced crystallinity of $Zn_xMg_{1-x}O$ by addition of O_2 during deposition as seen in Figure 4.13. Hence, optical band gap of ZnO_x could be increased without damaging crystal structure [64].

Deterioration of crystal structure with Mg doping resulted from the difference in electronegativity of the metal ions. In other words, oxygen prefers to make bonding with Mg rather than Zn due to lower electronegativity of Mg. Therefore, ZnO wurtzite structure diminished when Mg was involved in deposition. When oxygen was compensated by additional oxygen flow, crystal structure of ZnO was improved.
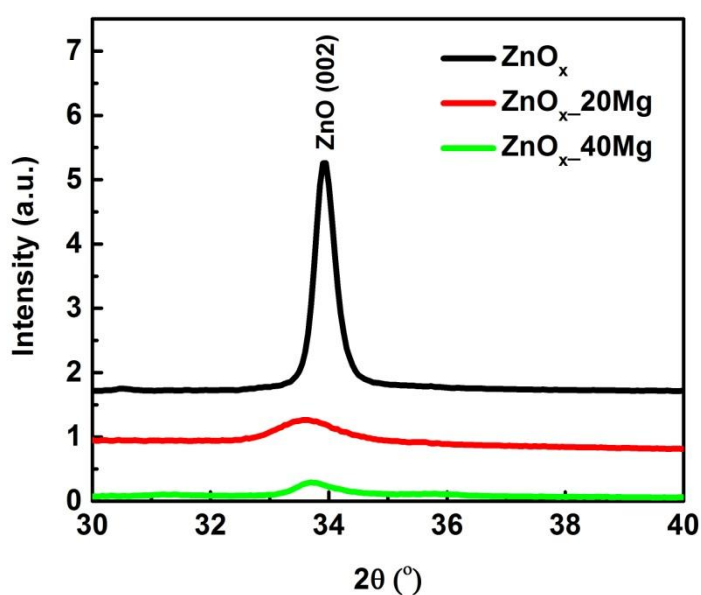
Figure 4.12. XRD spectrum of ZnO_x and $Zn_xMg_{1-x}O$ thin films

XRD spectrum of sample ZnOx_150Mg was obtained separately from other samples by grazing angle 0.03 ^{o} due to its small thickness. In the case of the ZnO_x_150Mg sample, spectrum was taken between 20 ^{o} and 70° because one of the MgO peak appearing around 63.2^o.

50
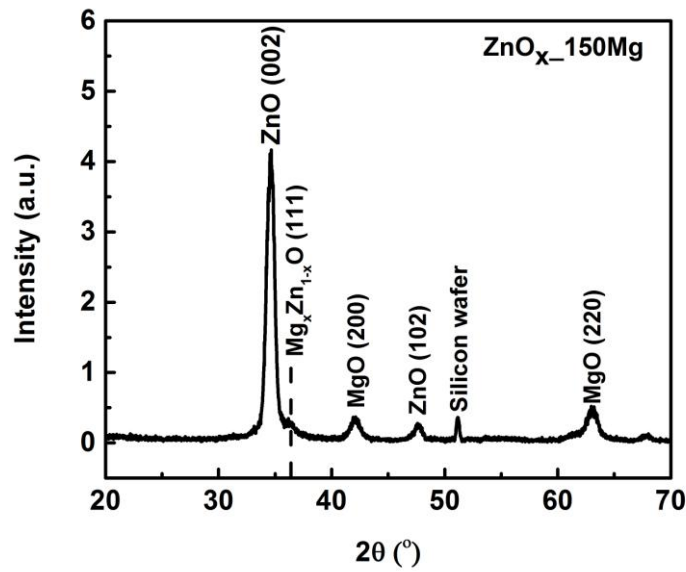
Figure 4.13. XRD spectrum of sample ZnO_x_150Mg

4.2.2. Effect of Introducing Oxygen during Sputtering on ZnO_x

ZnO_x thin films with various Zn/O_2 ratios were fabricated by magnetron and reactive RF sputtering techniques to observe the effect of stoichiometry on their crystal structure and optical properties.

Depositions were conducted under 4 mTorr and the power of ZnO_x target was set at 300 Watt for the fabrications. Deposition parameters are given in Figure 4.4.

Table 4.4. Deposition parameters of ZnO_x samples with different stoichiometry

Sample Name	RF Power of ZnO_x Target (Watt)	Ar Flow Rate (sccm)	O_2 Flow Rate (sccm)	Deposition Time (min)	Thinkness (nm)
ZnO_x	300	20	-	45	428.4
$ZnO_x\_1O_2$	300	19	1	45	337.4
$ZnO_x\_1O_2$	300	18	2	45	288.388

According to the ellipsometry results, extinction coefficient is zero for all samples and their refractive index decrease with increasing oxygen flow rate as shown in

Figure 4.14. Additionally, refractive index of ZnO_x in the visible wavelengths decreases gradually with increasing additional O_2 flow rate. ZnO_x without additional O_2 has already high transparency in the visible spectrum. Introducing additional O_2 during sputtering process does not have a considerable influence on transmission and reflection spectra, yet the thickness variations result in difference interference patterns as seen in Figure 4.14 (right).
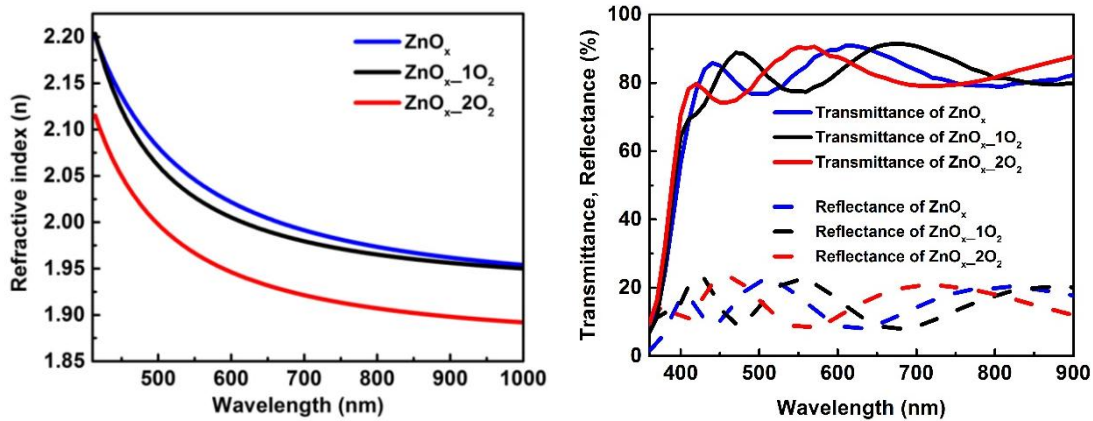
Figure 4.14. Refractive index (left), and transmittance and reflectance (right) spectra of ZnO_x samples with additional O_2 gas flow during sputtering

Crystal structure on ZnO_x was adversely influenced from introducing O_2 during deposition as seen in Figure 4.15. According to the XRD measurement of three samples, increasing O_2 ratio results in a broadening in the XRD peaks. It means a reduction in crystal size and most likely a decrease in electrical conductivity, too.
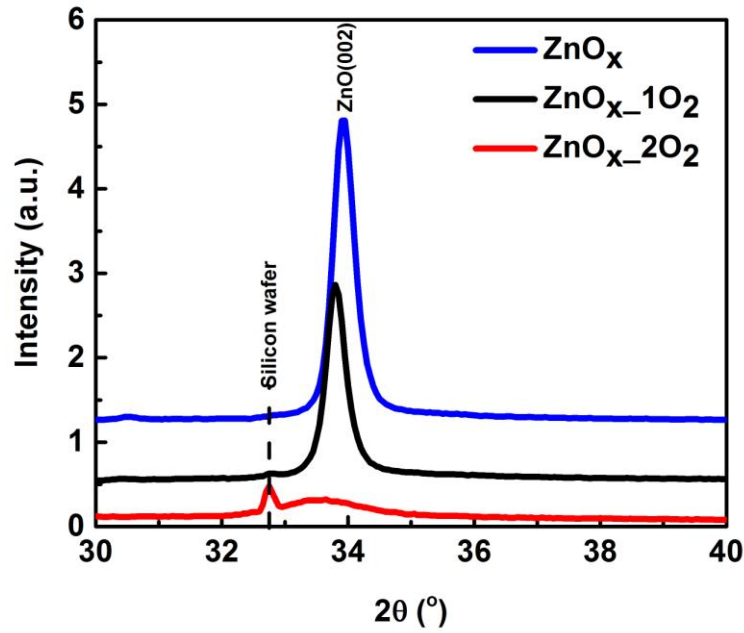
Figure 4.15. XRD spectrum of ZnO_x with additional oxygen gas flow during sputtering

4.2.3. Transmittance and Reflectance of ZnO_x with Various Thicknesses

Effect of thickness of ZnO_x on transmittance and reflectance was investigated. Depositions were carried out under 4 mTorr with the same parameters but different deposition times as shown in Table 4.5.

Table 4.5. Deposition parameters of ZnO_x fabricated with different thicknesses

Sample Name	RF Power of ZnO_x Target (Watt)	Ar Flow Rate (sccm)	Deposition Time (min)	Thinkness (nm)
ZnO_x	300	20	45	428.4
ZnOx_30min	300	20	30	269.1
ZnOx_15min	300	20	15	81.7

According to UV/Vis. spectrum of the fabricated thin films with different thicknesses show more than 80% transmittance in the visible spectrum. ZnO_x-10min sample with thickness of 81.5 nm has a higher transmittance in the near UV wavelengths.

53

However, it has a lower transmittance in the visible wavelengths with respect to the thicker samples since constructive interference dominates for that range as shown in Figure 4.16.
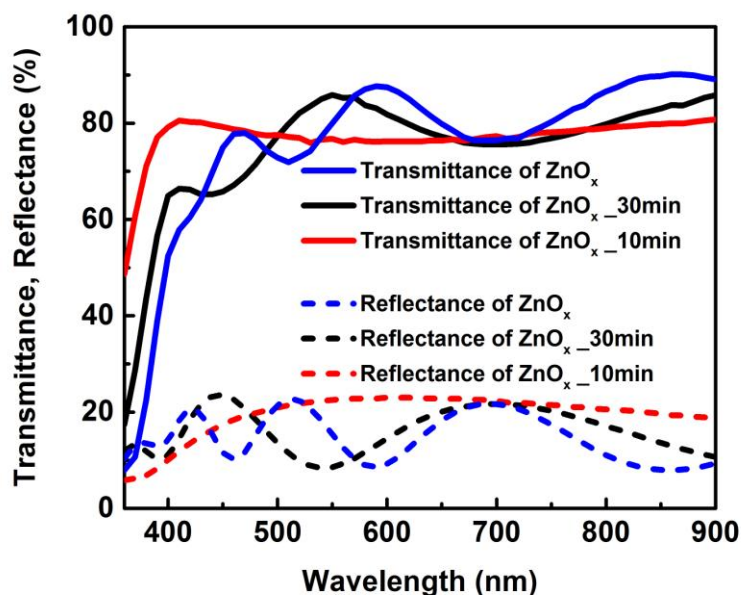
Figure 4.16. Transmittance and reflectance of ZnO_x with different thicknesses

4.2.4. Fabrication of Perovskite Solar Cell with sputtered ZnO_x and $Zn_xMg_{1-x}O$ ETL

ZnO_x and $Zn_xMg_{1-x}O$ thin films were implemented in the perovskite solar cell as ETL in device configuration of ITO/$Zn_xMg_{1-x}O$/perovskite/spiro:OMeTAD/Ag. A set of device with sputtered TiO_2 ETL were also fabricated for comparison purposes. While an efficiency of 0.8% was achieved in perovskite solar cells with sputtered TiO_2 ETL, the perovskite was degraded unexpectedly when $Zn_xMg_{1-x}O$ is used. In order to overcome the stability issue, ZnO_x was annealed on the hot plate at 250 ^{o}C for 30 min. Hot plate annealing of ZnO_x and $Zn_xMg_{1-x}O$ thin films prevented degradation problem as seen in Figure 4.17. Nevertheless, the efficiencies of the devices were well-below 1% as shown in Figure 4.18.

54
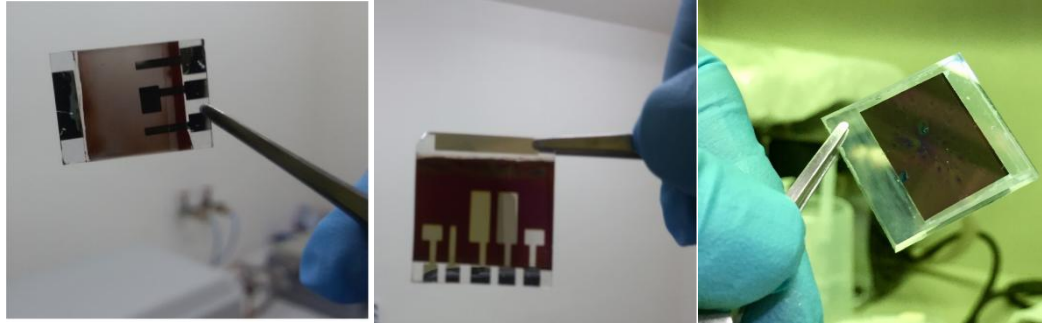
Figure 4.17. The perovskite solar cells incorporating as deposited ZnO_x (on the left), TiO_2 (in the middle) and annealed ZnO_x (on the right).

J-V results of the devices measured under 1 sun illumination are given in Table 4.6. According to J-V curves, perovskite solar cells with ZnO_x ETL has a lower J_{SC} and V_{OC} values compared to the ones with TiO_2 ETL, most likely due to degradation of perovskite on ZnO_x as shown in Figure. 4.18.
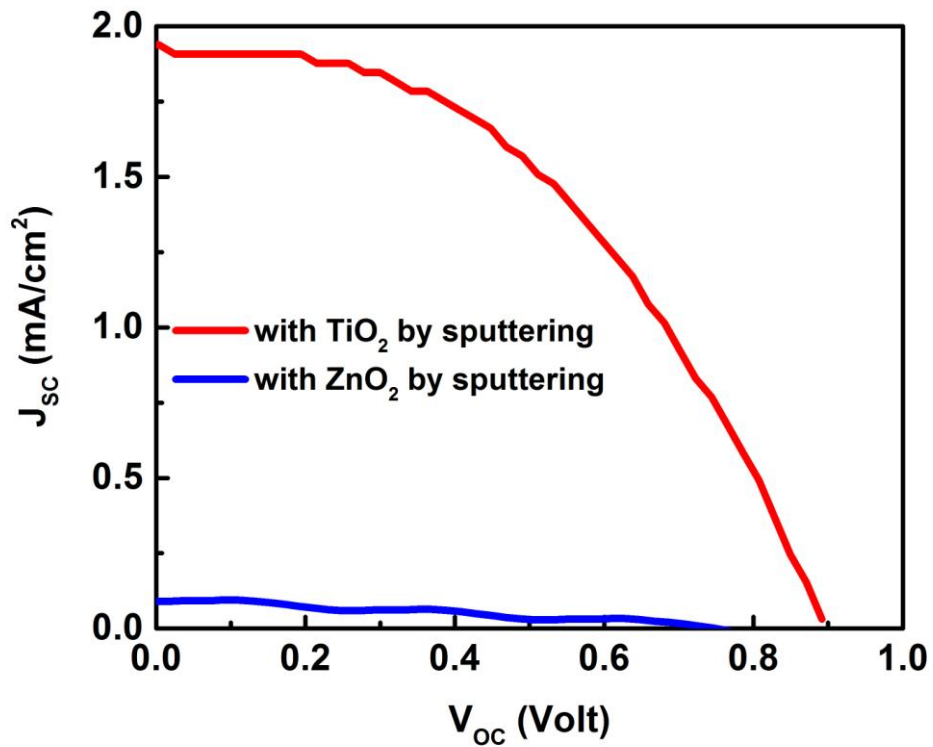
Figure 4.18. J-V curves of perovskite solar cells using ZnO_x and TiO_2 by sputtering

Table 4.6. Results of I-V measurement of perovskite solar cells with various ETL under 1 sun irradiance

Sample Name	J_{sc} (mA/cm^2)	V_{oc} (V)	Fill Factor (%)	Efficiency (%)
Perovskite with ZnO$_x$ ETL	0.1	0.812811	25.4	0.021
Perovskite with TiO$_2$ ETL	1.93	0.9	45.1	0.8

CHAPTER 5

CONCLUSIONS AND FUTURE STUDIES

For an efficient charge transport mechanism in heterojunction solar cells, charge transport materials with high conductivity, high transparency and well aligned energy bands with the adjacent materials are required. In this regard, it is necessary to alter electronic and optical properties of charge transport layers. In this thesis, it was aimed to engineer especially the energy band structure of MoO_x as HTL and $Zn_xMg_{1-x}O$ as ETL.

MoO_x is a natural n-type material, which result from being prone to have oxygen vacancy in its crystal structure. As a n-type material, its Fermi level shifts closer to the edge of the conduction band but its work function is to still high enough to be used as hole selective material in many heterojunction solar cells. However, it is critical to control the oxygen vacancy level to align the Fermi level of MoO_x with the valance band of absorber layer and the work function of electrodes for superior hole selection. In this study, MoO_x thin films were successfully fabricated by reactive DC sputtering and reactive RF sputtering. Then, the ones fabricated by reactive RF sputtering were intentionally exposed to post treatments which are RTA annealing, UV/O_3 and hot plate annealing to control the oxygen defect sites. The defect states in the band gap of the materials were measured by XPS. It was concluded that as deposited MoO_x samples already had oxygen defects even without any post treatment. Then, they were annealed at different temperatures and different ambient to control the defects. According to the results, oxygen vacancy formation can be controlled by annealing temperature under nitrogen flow. However, it is not very

controllable when there is oxygen in the ambient since oxygen vacancy formation is reversible. ZnO_x is another material which was studied in the scope of this thesis. ZnO_x is an excellent material due to its high transparency in the visible spectrum and its conductivity. Also, it is relatively cheaper than most of the conventional ETLs such as TiO_2. Relying on this motivation, ZnO_x and $Zn_xMg_{1-x}O$ thin films were investigated in this study. It was first aimed to tune optical band gap by Mg doping. It was proven that increasing the concentration of Mg increased the optical band gap but it damaged the crystal structure of ZnO_x, as well. This is not very desired for a charge transport layer in terms of electrical conductivity. However, the crystal structure was enhanced when doping was carried out under additional oxygen gas flow during deposition. This is one of the most important conclusions of the experiments on ZnO_x since it will allow tuning band gap of ZnO_x without any damage in crystal structure.

Finally, perovskite was deposited on as deposited ZnO_x and $Zn_xMg_{1-x}O$ layers to test their performance but perovskite degraded unexpectedly. However, the stability of the perovskite was improved when ZnO_x and $Zn_xMg_{1-x}O$ layers were annealed on hot plate.

In the future studies, firstly, ZnO_x and $Zn_xMg_{1-x}O$ ETLs and MoO_x HTL can be characterized by UPS to obtain their energy band diagrams. Secondly, each of the transport materials studied in this thesis can be implemented in various heterojunction solar cells. ZnO_x was already utilized as ETL in the perovskite solar cell but MoO_x has not been tested although it was extensively studied. Furthermore, other transport materials such as TiO_2 and NiO_x can be also investigated as charge transport materials.

REFERENCES

[1]   United Nations, "World Population Prospect: The 2015 Revision,World Population 2015 Wallchart. ST/ESA/SER.A/378," p. 2, 2015.

[2]   BP, "BP Statistical Review of World Energy About this review Contents," no. June, pp. 1–48, 2013.

[3]   "History of Solar Cells_ How Technology Has Evolved _ Solar Power Authority." .

[4]   D. M. Chapin, C. S. Fuller, and G. L. Pearson, "A New Silicon p-n Junction Photocell for Converting Solar Radiation into Electrical Power," *J. Appl. Phys.*, vol. 25, no. 5, p. 676, 1954.

[5]   X. He and H. Zervos, "Perovskite Photovoltaics 2016-2026:Technologies, Markets, Players." 2016.

[6]   "National Renewable Energy Laboratory." [Online]. Available: http://www.nrel.gov/.

[7]   I. B. Gisbert, "Study Of Different Electron And Hole Transporting Materials For Quantum Dot-Sensitized Solar Cells Irene Barceló Gisbert," 2015.

[8]   a. L. D. and J.C.Joshi, "Semiconducting Transparent Thin Films," *J. Mater. Sci.*, no. 19, pp. 1–23, 1984.

[9]   E. Fortunato, D. Ginley, H. Hosono, and D. C. Paine, "TransparentConducting Oxidesfor Photovoltaics," *MRS Bull.*, vol. 32, no. March, pp. 242–247, 2007.

[10]   M. T. Bhatti, A. M. R. Rana, A. F. Khan, and M. I. Ansari, "Effect of Annealing on Electrical Properties of Indium Tin Oxide (ITO) Thin Films," *Pakistan J. Appl. Sci.*, vol. 5, pp. 570–573, 2002.

[11] H.-H. Wang, Q. Chen, H. Zhou, L. Song, Z. S. Louis, N. De Marco, Y. Fang, P. Sun, T.-B. Song, H. Chen, and Y. Yang, "Improving the TiO2 electron transport layer in perovskite solar cells using acetylacetonate-based additives," *J. Mater. Chem. A*, vol. 3, no. 17, pp. 9108–9115, 2015.

[12] Q. Liu, "Optimization and Characterization of Transparent Oxide Layers for CIGS solar cells fabrication," 2007.

[13] T. D. No and B. Link, *Studies of Charge Transport and Energy Level in Solar Cells Based on Polymer / Fullerene Bulk Heterojunction Abay Gadisa*, no. 1056. 2006.

[14] S. Huang, W. Luo, and Z. Zou, "Band positions and photoelectrochemical properties of Cu 2 ZnSnS 4 thin films by the ultrasonic spray pyrolysis method," *J. Phys. D. Appl. Phys.*, vol. 46, no. 23, p. 235108, Jun. 2013.

[15] Z. Liang, Q. Zhang, L. Jiang, and G. Cao, "ZnO Cathode Buffer Layers for Inverted Polymer Solar Cells," *Energy Environ. Sci.*, vol. 8, pp. 3442–3476, 2015.

[16] M. Ohring, *Material Science of Thin Films*, 2nd ed. 2001.

[17] T. English, *Physical Sputtering and Sputter*. 2010.

[18] S. Series, *Reactive Sputter Deposition*.

[19] H. H. Perkampus, "UV-VIS Spectroscopy and Its Applications." .

[20] G. E. Jellison, "Data Analysis : a Tutorial," 2000.

[21] T. Model, "Cauchy and related Empirical Dispersion Formulae for Transparent Materials," 1836.

[22] G. . David Krupadanam, D. Vijaya Prasad, K. Reddy, and C. Sudhakar, "Analytical Chemistry." .

[23] V. M. Huxter and V. M. Huxter, "Optical and Material Properties of Colloidal by," 2009.

[24] B. D. Cullity, *Elements of X-Ray Diffraction*. 1956.

[25] P. Van der Heide, "X-ray Photoelectron Spectroscopy: An introduction to Principles and Practices." John Wiley& Sons, Inc., New Jersey, 1962.

[26] C. Battaglia, X. Yin, M. Zheng, I. D. Sharp, T. Chen, S. Mcdonnell, A. Azcatl, C. Carraro, B. Ma, R. Maboudian, R. M. Wallace, and A. Javey, "Hole Selective MoO," 2014.

[27] K. Mahmood, B. S. Swain, and A. Amassian, "16.1% Effi cient Hysteresis-Free Mesostructured Perovskite Solar Cells Based on Synergistically Improved ZnO Nanorod Arrays," *Adv. Energy Mater.*, 2015.

[28] S. Seo, I. J. Park, M. Kim, S. Lee, C. Bae, H. S. Jung, N.-G. Park, J. Y. Kim, and H. Shin, "An ultra-thin, un-doped NiO hole transporting layer of highly efficient (16.4%) organic-inorganic hybrid perovskite solar cells," *Nanoscale*, vol. 8, p. 11403, 2016.

[29] M. Satake and Y. Mido, "Chemistry Of Transition Elements." Discovery Publishing House.

[30] M. Miyauchi, A. Nakajima, A. Fujishima, K. Hashimoto, and T. Watanabe, "Photoinduced Surface Reactions on TiO 2 and SrTiO 3 Films: Photocatalytic Oxidation and Photoinduced Hydrophilicity," no. 25, pp. 3–5, 2000.

[31] Y. Liu and R. E. Allen, "Electronic structure of," vol. 52, no. 19. pp. 991–994, 1995.

[32] M. T. Greiner, M. G. Hlander, W.-M. Tang, Z.-B. Wang, J. Qui, and Z.-H. Lu, "Universal energy-level alignment of molecules on metal oxides," *Nat. Mater.*, vol. 11, no. 1, pp. 76–81, 2012.

[33] Z. Zhang, Y. Xiao, H.-X. Wei, G.-F. Ma, S. Duhm, Y.-Q. Li, and J.-X. Tang,

"Impact of Oxygen Vacancy on Energy-Level Alignment at MoO x /Organic Interfaces," *Appl. Phys. Express*, vol. 6, no. 9, p. 95701, 2013.

[34] F. Xie and W. C. H. Choy, "Hydrogen metal oxide bronzes for efficient hole transport layers," pp. 2–4.

[35] Y. Guo and J. Robertson, "Origin of the High work function and high conductivity of MoO 3," pp. 1–10.

[36] S. Malhotra and L. Goswami, "Study and Analyze the Effect of Hole Transport Layer on the Power Conversion Efficiency of P3HT : PCBM based Organic Solar Cell," vol. 3, no. 9, pp. 2012–2015, 2014.

[37] S. Shao, J. Liu, J. Bergqvist, S. Shi, C. Veit, U. Würfel, Z. Xie, and F. Zhang, "In Situ Formation of MoO3 in PEDOT:PSS Matrix: A Facile Way to Produce a Smooth and Less Hygroscopic Hole Transport Layer for Highly Stable Polymer Bulk Heterojunction Solar Cells," *Adv. Energy Mater.*, vol. 3, no. 3, pp. 349–355, 2013.

[38] C. Liu, Z. Su, W. Li, F. Jin, B. Chu, J. Wang, H. Zhao, C. S. Lee, J. Tang, and B. Kang, "Improved performance of perovskite solar cells with a TiO2/MoO3 core/shell nanoparticles doped PEDOT:PSS hole-transporter," *Org. Electron.*, vol. 33, pp. 221–226, 2016.

[39] F. Hou, Z. Su, F. Jin, X. Yan, L. Wang, H. Zhao, J. Zhu, B. Chu, and W. Li, "Efficient and stable planar heterojunction perovskite solar cells with an MoO3/PEDOT:PSS hole transporting layer," *Nanoscale*, vol. 7, no. 21, pp. 9427–9432, 2015.

[40] S. S. Electrochemistry, S. B. Academy, T. Ivanova, and B. Academy, "Spectroscopic ellipsometry study of CVD molybdenum oxide films : Effect of temperature," no. January 2002, 2016.

[41] K. Mahmood, B. S. Swain, and A. Amassian, "16.1% Efficient Hysteresis- Free Mesostructured Perovskite Solar Cells Based on Synergistically Improved ZnO Nanorod Arrays," *Adv. Energy Mater.*, vol. 5, no. 17, 2015.

[42] S. K. Singh and R. Chauhan, "Study of Optical Properties of Transition Metal Oxides on the Basis of Energy Band and Energy State Analysis," pp. 37–40, 2014.

[43] C. Jagadish and S. J. Pearton, Eds., *Zinc Oxide Bulk, Thin Films and Nanostructures*. 2011.

[44] J. Dong, J. Shi, D. Li, Y. Luo, and Q. Meng, "Controlling the conduction band offset for highly efficient ZnO nanorods based perovskite solar cell," *Appl. Phys. Lett.*, vol. 107, no. 7, p. 73507, 2015.

[45] S. J. Pearton, D. P. Norton, K. Ip, Y. W. Heo, and T. Steiner, "Recent progress in processing and properties of ZnO," *Prog. Mater. Sci.*, vol. 50, no. 3, pp. 293–340, 2005.

[46] W. Walukiewicz, "Defect formation and diffusion in heavily doped semiconductors," *Phys. Rev. B*, vol. 50, no. 8, pp. 5221–5225, Aug. 1994.

[47] M. Asghar, K. Mahmood, and M. A. Hasan, "Investigation of Source of N-Type Conductivity in Bulk ZnOTitle," *Key Eng. Mater.*, vol. 510–511, pp. 227–232, 2012.

[48] L. Liu, Z. Mei, A. Tang, A. Azarov, A. Kuznetsov, Q. K. Xue, and X. Du, "Oxygen vacancies: The origin of n-type conductivity in ZnO," *Phys. Rev. B - Condens. Matter Mater. Phys.*, vol. 93, no. 23, 2016.

[49] X. Li, J. Song, Y. Liu, and H. Zeng, "Controlling oxygen vacancies and properties of ZnO," *Curr. Appl. Phys.*, vol. 14, no. 3, pp. 521–527, 2014.

[50] C. G. de Walle, "Hydrogen as a Cause of Doping in Zinc Oxide," *Phys. Rev. Lett.*, vol. 85, no. 5, pp. 1012–1015, Jul. 2000.

[51] A. Janotti and C. G. Van De Walle, "Fundamentals of zinc oxide as a semiconductor," vol. 72, 2009.

[52] S. J. Jokela and M. D. Mccluskey, "Structure and stability of O - H donors in ZnO from high-pressure and infrared spectroscopy," pp. 1–4, 2005.

[53] H. Cheun, C. Fuentes-Hernandez, Y. H. Zhou, W. J. Potscavage, S. J. Kim, J. Shim, a Dindar, and B. Kippelen, "Electrical and Optical Properties of ZnO Processed by Atomic Layer Deposition in Inverted Polymer Solar Cells," *J. Phys. Chem. C*, vol. 114, pp. 20713–20718, 2010.

[54] M. A. Ibrahem, H. Y. Wei, M. H. Tsai, K. C. Ho, J. J. Shyue, and C. W. Chu, "Solution-processed zinc oxide nanoparticles as interlayer materials for inverted organic solar cells," *Sol. Energy Mater. Sol. Cells*, vol. 108, pp. 156–163, 2013.

[55] L. C. Olsen, W. Lei, F. W. Addis, W. N. Shafarman, M. A. Contreras, and K. Ramanathan, "High efficiency CIGS and CIS cells with CVD ZnO buffer layers," in *Photovoltaic Specialists Conference, 1997., Conference Record of the Twenty-Sixth IEEE*.

[56] A. Gupta and A. D. Compaan, "14% CdS/CdTe Thin Film Cells with ZnO:Al TCO," *MRS Proc.*, vol. 763, 2003.

[57] S. Lattante, "Electron and Hole Transport Layers: Their Use in Inverted Bulk Heterojunction Polymer Solar Cells," *Electronics*, vol. 3, no. 1, pp. 132–164, 2014.

[58] X. Yu, X. Yu, Z. Hu, J. Zhang, G. Zhao, and Y. Zhao, "Effect of sol–gel derived ZnO annealing rate on light-trapping in inverted polymer solar cells," 2013.

[59] N. K. Elumalai, C. Vijila, R. Jose, K. Z. Ming, A. Sahad, and S. Ramakrishnaa, "Simultaneous improvements in power conversion efficiency and operational stability of polymer solar cells by interfacial engineering," *Phys. Chem. Chem. Phys.*, vol. 15, no. 43, pp. 19057–19064, 2013.

[60] Z. Hu, J. Zhang, and Y. Zhu, "Inverted polymer solar cells with a boron-doped zinc oxide layer deposited by metal organic chemical vapor deposition," *Sol. Energy Mater. Sol. Cells*, vol. 117, pp. 610–616, Oct. 2013.

[61] Z.-L. Tseng, C.-H. Chiang, and C.-G. Wu, "Surface Engineering of ZnO Thin Film for High Efficiency Planar Perovskite Solar Cells.," *Sci. Rep.*, vol. 5, p. 13211, 2015.

[62] S. Kumar, A. Kumar, F. Singh, and A. Kapoor, "Preparation of Mg-doped ZnO nanoparticles by Sol-gel method and their Optical & structural properties Table 1 : c-axis lattice constant (Å), Stress , porosity (P), average crystallite size (D) and Optical band gap of the samples . Parameters c-axis ," pp. 1–2, 2013.

[63] X. Xu, H. Zhang, J. Shi, J. Dong, Y. Luo, D. Li, and Q. Meng, "Highly efficient planar perovskite solar cells with a TiO2 /ZnO electron transport bilayer," *J. Mater. Chem. A*, vol. 3, no. 38, pp. 19288–19293, 2015.

[64] A. S. Asvarov, Ss. Makhmodov, A. K. Abduev, M. . Aliev, and B. . Bilalov, "Structural and Optical Properties of Mg Doped ZnO Thin Films Deposited by DC Magnetron Sputtering," *J. Nano Electron. Phys.*, vol. 8, no. 4, pp. 2–5, 2016.

[67] Henrich, V (1988). Surface and Near-surface Chemistry of Oxide Materials. Amsterdam: Elsevier. pp. 23–309.